Joint Waveform and Filter Designs for STAP-SLP-Based MIMO-DFRC Systems

Rang Liu, *Graduate Student Member, IEEE*, Ming Li, *Senior Member, IEEE*, Qian Liu, *Member, IEEE*, and A. Lee Swindlehurst, *Fellow, IEEE*

***Abstract*— Dual-function radar-communication (DFRC), which can simultaneously perform both radar and communication functionalities using the same hardware platform, spectral resource and transmit waveform, is a promising technique for realizing integrated sensing and communication (ISAC). Space-time adaptive processing (STAP) in multi-antenna radar systems is the primary tool for detecting moving targets in the presence of strong clutter. The idea of joint spatial-temporal optimization in STAP-based radar systems is consistent with the concept of symbol-level precoding (SLP) for multi-input multi-output (MIMO) communications, which optimizes the transmit waveform for each of the transmitted symbols. In this paper, we combine STAP and SLP and propose a novel STAP-SLP-based DFRC system that enjoys the advantages of both techniques. The radar output signal-to-interference-plus-noise ratio (SINR) is maximized by jointly optimizing the transmit waveform and receive filter, while satisfying the communication quality-of-service (QoS) constraint and various waveform constraints including constant-modulus, similarity and peak-to-average power ratio (PAPR). An efficient algorithm framework based on majorization-minimization (MM) and non-linear equality constrained alternative direction method of multipliers (neADMM) methods is proposed to solve these complicated non-convex optimization problems. Simulation results verify the effectiveness of the proposed STAP-SLP-based MIMO-DRFC scheme and the associate algorithms.**

***Index Terms*— Dual-functional radar-communication (DFRC), integrated sensing and communication (ISAC), space-time adaptive processing (STAP), symbol-level precoding (SLP), multi-input multi-output (MIMO).**

Manuscript received August 19, 2021; revised December 5, 2021; accepted January 14, 2022. Date of publication March 2, 2022; date of current version May 18, 2022. This work was supported in part by the National Natural Science Foundation of China under Grant 61971088, Grant 62071083, Grant U1808206, and Grant U1908214; in part by the Natural Science Foundation of Liaoning Province under Grant 2020-MS-108; in part by the Fundamental Research Funds for the Central Universities under Grant DUT20GJ214 and Grant DUT21GJ208; and in part by the Dalian Science and Technology Innovation Project under Grant 2020JJ25CY001. The work of A. Lee Swindlehurst was supported by the U.S. National Science Foundation under Grant CCF-2008714. *(Corresponding author: Ming Li.)*

Rang Liu and Ming Li are with the School of Information and Communication Engineering, Dalian University of Technology, Dalian 116024, China (e-mail: liurang@mail.dlut.edu.cn; mli@dlut.edu.cn).

Qian Liu is with the School of Computer Science and Technology, Dalian University of Technology, Dalian 116024, China (e-mail: qianliu@dlut.edu.cn).

A. Lee Swindlehurst is with the Center for Pervasive Communications and Computing, University of California at Irvine, Irvine, CA 92697 USA (e-mail: swindle@uci.edu).

Color versions of one or more figures in this article are available at https://doi.org/10.1109/JSAC.2022.3155501.

Digital Object Identifier 10.1109/JSAC.2022.3155501

I. Introduction

With the exponential growth of wireless services and the plethora of wireless devices, spectral resources are becoming increasingly scarce, motivating the urgent need for advanced spectrum sharing technologies. The radar frequency bands, which have large portions of available spectrum, are promising candidates for sharing with various communication systems. Spectrum sharing between radar and communication systems is consistent with the on-going convergence of integrated sensing and communication (ISAC) functions [1]–[5], and has led to substantial research interest in the coexistence, cooperation, and co-design of these two systems [6]–[9].

Unlike radar and communication coexistence/cooperation (RCC) which requires interference management and side-information exchange, ISAC enables the co-design of the sensing and communication functions. By efficiently sharing the same spectral resources, a given hardware platform, and a joint signal processing framework, ISAC can realize both sensing and communication functions and even result in mutual benefits [10]–[12]. ISAC can provide considerable gains in terms of spectral/energy/hardware/cost efficiency and has attracted significant research interest in both academia and industry. It is believed that ISAC will become a promising technology in future wireless communication systems to support various application scenarios, such as vehicular networks, smart cities, environmental monitoring, remote sensing, internet-of-things (IoT), etc. Moreover, ISAC is also considered to be a key enabling technology for next-generation cellular and Wi-Fi systems.

ISAC systems can have different levels of integration. In a looser configuration, these two functions are just physically integrated on a given platform, but employ different sets of hardware components and/or transmit waveforms. This loose integration may only offer limited benefits such as lower signalling overhead and better interference management. The rationale of ISAC is that sensing and communication functions are tightly integrated and can be simultaneously performed using a fully-shared transmitter/receiver, the same frequency bands, and the same dual-functional waveforms, which allows for significantly greater improvements in efficiency [10]. An ISAC system with such tight integration is more often referred to as a dual-functional radar-communication (DFRC) system in the literature [13]–[19]. The main goal of a DFRC system is to generate novel dual-functional waveforms to simultaneously perform radar sensing and communication

functions. Multi-input multi-output (MIMO) architectures have been widely employed in DFRC systems to improve the spatial-domain waveform diversity for radar sensing [20], as well as to achieve beamforming gains and spatial multiplexing for multi-user communications. Thanks to advancements in fully co-designed radar sensing and communication waveforms, MIMO-DFRC is recognized as a key enabler for ISAC systems to significantly improve spectral efficiency, reduce device size, cost and power consumption, and enhance performance, all of which are the focus of this paper.

Due to the inherently conflicting requirements of radar sensing and communication functions, transmit waveform design is pivotal in pursuing better performance trade-offs for MIMO-DFRC systems [4]. Therefore, many researchers have devoted their study to transmit waveform designs with various radar sensing and communication metrics [13]–[19], [21]–[23], e.g., average transmit beampattern, signal-to-interference-plus-noise ratio (SINR), mutual information, similarity with a reference waveform, achievable rate, etc. However, most existing research for implementing MIMO-DFRC only focuses on designing the spatial second-order statistics of the transmit waveforms and ignores the Doppler bin in the temporal domain. Moreover, an overly simplified radar sensing environment without clutter is usually assumed in the existing literature. Therefore, the target detection performance of these designs may be not satisfactory, and could even be unacceptable in a hostile radar sensing environment.

Space-time adaptive processing (STAP) is an effective technique for achieving adaptive clutter suppression and better target detection in multi-antenna radars [24]–[31]. STAP optimizes the spatial-temporal transmit waveforms rather than their spatial second-order statistics to maximize the output SINR performance, for the purpose of suppressing the clutter. Since the waveform optimization exploits degrees of freedom (DoFs) in both the spatial and temporal domains, the performance of identifying a target in the presence of strong clutter over widely spread ranges and angular regions is significantly improved. Using a priori knowledge about the clutter, e.g., the clutter covariance matrix (CCM) [32]–[34], there has been growing interest in designing the waveforms using knowledge-aided techniques to improve the STAP performance.

In communications applications, the recently emerged symbol-level precoding (SLP) technique also exploits available DoFs in both the spatial and temporal domains to improve link performance. In particular, SLP designs the transmit precoder in each time slot (i.e., the transmit waveform samples) based on the specific transmitted symbols themselves rather than their second-order statistics. The transmit precoder/waveform can be designed to convert harmful interference into beneficial signal power, and such constructive interference (CI) can improve the communication quality-of-service (QoS) [35]–[40]. The flexibility offered by SLP in the time domain and its ability to achieve better communication QoS make SLP techniques a promising candidate for MIMO-DFRC systems, in which the transmit waveform used for radar sensing simultaneously carries information symbols for wireless communications.

Very limited research has been conducted to exploit SLP for joint radar-communication systems. In prior work [6], the SLP technique was employed in an RCC system to take advantage of interference exploitation. However, in RCC systems, the SLP design only optimizes the communication performance metric while simultaneously suppressing interference to the radar system regardless of the specific radar waveforms. Another very recent work [41] introduces SLP to MIMO-DFRC systems for the first time and illustrates that SLP can provide more accurate angle estimation and better target detection performance, as well as lower symbol-error-rate (SER) for multi-user communications compared with conventional block-level precoding (BLP) schemes. Nevertheless, this work only optimizes the transmit waveform based on the beampattern similarity metric, and does not consider the properties of the radar waveform in the temporal-domain. The spatial-temporal receive filter and clutter suppression are also not taken into account. Therefore, the flexibility of SLP has not been fully exploited for MIMO-DFRC systems in the prior literature.

Motivated by the above discussion, in this paper we leverage STAP and CI-based SLP techniques for implementing MIMO-DFRC to combine their advantages for both radar and communication functions. In particular, we consider a multi-antenna base station (BS) that simultaneously uses active sensing to detect a target in the presence of strong signal-dependent clutter and transfers information symbols to multiple single-antenna users. The transmit waveform and receive filter of the BS are jointly optimized to maximize the radar output SINR under communication QoS constraints and several different radar waveform constraints. The main contributions can be summarized as follows:

- For the first time, we integrate STAP and SLP techniques to implement MIMO-DFRC in order to achieve considerable improvements in target detection performance in the presence of strong clutter, as well as to boost multi-user communication performance by converting harmful interference into beneficial signal power. Compared with conventional BLP-based waveform designs, STAP and SLP techniques impose quite different radar sensing and communication constraints in the temporal domain and consequently result in brand-new waveform design problems.
- We first model the joint transmit waveform and receive filter optimization problem for the novel STAP-SLP-based MIMO-DFRC system. Then, focusing on the constant-modulus constrained waveform design problem, we employ the majorization-minimization (MM) method and derive a tractable surrogate function, and then exploit the novel nonlinear equality constrained alternative direction method of multipliers (neADMM) method to convert the problem into manageable sub-problems. Detailed derivations and efficient algorithms are developed to obtain the optimal solutions for each sub-problem.
- Next, we generalize the proposed MM-neADMM algorithm to waveform designs with constant-modulus similarity and peak-to-average power ratio (PAPR) constraints.

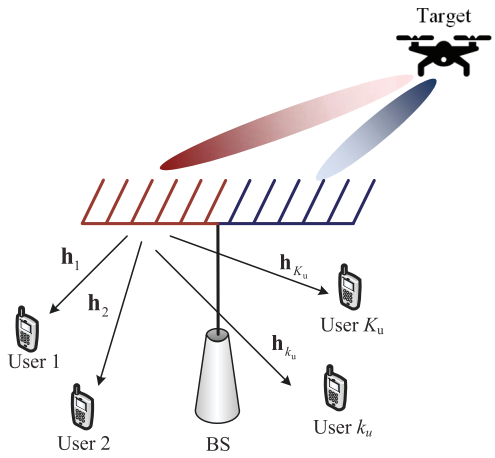

Fig. 1. The considered MIMO-DFRC system.

- We provide extensive simulation results to verify the advantages of jointly exploiting STAP and CI-based SLP techniques to implement MIMO-DFRC and demonstrate the effectiveness of the proposed algorithms under different waveform constraints.

Notation: Boldface lower-case and upper-case letters indicate column vectors and matrices, respectively. $(\cdot)^T$ and $(\cdot)^H$ denote the transpose and the transpose-conjugate operations, respectively. $\mathbb{C}$ and $\mathbb{R}$ denote the sets of complex numbers and real numbers, respectively. $|a|$, $\|\mathbf{a}\|$, and $\|\mathbf{a}\|_\infty$ are the magnitude of a scalar a, the 2-norm of a vector $\mathbf{a}$, and the infinity norm of a vector $\mathbf{a}$, respectively. $\angle a$ is the angle of complex-valued a. $\Re\{a\}$ and $\Im\{a\}$ denote the real and imaginary part of a scalar a, respectively. $\otimes$ denotes the Kronecker product. $\mathbb{E}\{\cdot\}$ denotes the expectation operation. $\mathrm{Tr}\{\mathbf{A}\}$ takes the trace of a matrix $\mathbf{A}$ and $\mathrm{vec}\{\mathbf{A}\}$ vectorizes the matrix $\mathbf{A}$. $\mathbf{I}_M$ indicates an $M \times M$ identity matrix.

II. System Model and Problem Formulation

Consider a colocated narrowband DFRC system as shown in Fig. 1, where a BS is equipped with N_t transmit antennas and N_r receive antennas arranged as uniform linear arrays (ULAs) with antenna spacing d_t and d_r, respectively. The BS aims to detect a target in the presence of strong signal-dependent clutter and simultaneously provide downlink wireless communication services to K_u single-antenna users. In order to detect moving targets in the presence of strong signal-dependent clutter over widely spread ranges, angular regions and Doppler frequencies, the BS uses STAP to exploit all available DoFs in both the spatial and temporal domains. In other words, the BS, which can be thought of as a colocated MIMO radar, uses STAP to jointly design the spatial-temporal transmit waveform and receive filter for achieving better target detection and clutter suppression performance. Meanwhile, in order to simultaneously realize satisfactory communication performance, the information symbols are carried by the same transmit waveforms using CI-based SLP for better communication QoS.

We assume that the radar is interrogating a moving target at the azimuth direction θ_0 with a speed v_0, in the presence of strong clutter from neighboring range cells. Assume that a burst of M pulses is transmitted from the radar transmitter in a coherent processing interval (CPI) with a constant pulse repetition frequency (PRF) f_r, and hence a constant pulse repetition interval (PRI) $T_\mathrm{r} = 1/f_\mathrm{r}$. Let $\widetilde{x}_{n_\mathrm{t}}(t)$ be the transmitted waveform of the n_t-th transmit antenna, $n_\mathrm{t} = 1, \ldots, N_\mathrm{t}$, and define $\widetilde{\mathbf{x}}(t) \triangleq [\widetilde{x}_1(t), \ldots, \widetilde{x}_{N_\mathrm{t}}(t)]^T$. It should be emphasized that, due to the use of SLP, the transmit waveforms vary from pulse-to-pulse to realize the multi-user communications, unlike what is assumed in most conventional MIMO radar systems that repeatedly transmit the same pulse.

A. Radar Received Signal and Radar Performance Metric

The radar received signal $\mathbf{y}$ in the cell under test (CUT) can be expressed as one of two possible hypotheses:

$$\begin{cases} \mathcal{H}_0 : \mathbf{y} = \mathbf{y}_\mathrm{c} + \mathbf{z}, \\ \mathcal{H}_1 : \mathbf{y} = \mathbf{y}_0 + \mathbf{y}_\mathrm{c} + \mathbf{z}, \end{cases} \tag{1}$$

where $\mathbf{y}_0$ and $\mathbf{y}_\mathrm{c}$ respectively represent the received signal returns reflected from the target and the clutter, and the vector $\mathbf{z} \sim \mathcal{CN}(0, \sigma_\mathrm{r}^2\mathbf{I})$ denotes additive white Gaussian noise (AWGN) at the receive antennas. The radar system decides whether a target is observed by testing the binary hypotheses in (1).

The received echo from the target with direction of arrival (DoA) θ_0 can be written as

$$\widetilde{\mathbf{y}}_0(t) = \alpha_0 \mathbf{b}(\theta_0)\mathbf{a}^H(\theta_0)\widetilde{\mathbf{x}}(t-\tau_0)e^{j2\pi(f_0+f_\mathrm{d})(t-\tau_0)}, \tag{2}$$

where α_0 represents the target amplitude with $\mathbb{E}\{|\alpha_0|^2\} = \sigma_0^2$, the scalar τ_0 is the two-way propagation delay, f_0 is the carrier frequency of the transmit waveform, and $f_\mathrm{d} = 2v_0/\lambda$ is the target Doppler frequency with $\lambda = c/f_0$ denoting the wavelength and c representing the speed of light. The vectors $\mathbf{b}(\theta)$ and $\mathbf{a}(\theta)$ are the steering vectors for the receive and transmit signals at angle θ, respectively:

$$\mathbf{b}(\theta) \triangleq \left[1, e^{j2\pi f_\mathrm{s}}, \ldots, e^{-j2\pi(N_\mathrm{r}-1)f_\mathrm{s}}\right]^T, \tag{3a}$$

$$\mathbf{a}(\theta) \triangleq \left[1, e^{j2\pi f_\mathrm{s} d_\mathrm{t}/d_\mathrm{r}}, \ldots, e^{-j2\pi(N_\mathrm{t}-1)f_\mathrm{s} d_\mathrm{t}/d_\mathrm{r}}\right]^T, \tag{3b}$$

where $f_\mathrm{s} \triangleq d_\mathrm{r}\sin\theta/\lambda$ denotes the normalized spatial frequency.

The received signal is first down-converted to baseband and then passed through an analog-to-digital converter. For simplicity, we absorb the constant phase terms associated with τ_0 into the target amplitude and assume the intra-pulse Doppler shift is negligible. Thus, for the m-th pulse, the baseband digital samples at the considered range gate can be expressed in matrix form as

$$\mathbf{Y}_{0,m} = \alpha_0 e^{j2\pi(m-1)f_\mathrm{d}T_\mathrm{r}}\mathbf{b}(\theta_0)\mathbf{a}^H(\theta_0)\mathbf{X}_m, \tag{4}$$

where $\mathbf{X}_m = [\widetilde{\mathbf{x}}_{m,1}, \ldots, \widetilde{\mathbf{x}}_{m,N_\mathrm{t}}]^T \in \mathbb{C}^{N_\mathrm{t}\times N}$ denotes the waveform matrix, and $\widetilde{\mathbf{x}}_{m,n_\mathrm{t}} \in \mathbb{C}^N$ is a vector of samples of $\widetilde{x}_{n_\mathrm{t}}(t)$, where N samples are taken per pulse. Then, we vectorize the received baseband digital samples in a CPI by letting $\mathbf{y}_0 = [\mathrm{vec}\{\mathbf{Y}_{0,1}^T\}^T, \ldots, \mathrm{vec}\{\mathbf{Y}_{0,M}^T\}^T]^T$, which can be expressed as

$$\mathbf{y}_0 = \alpha_0 \overline{\mathbf{X}}\big(\mathbf{d}(f_\mathrm{d}) \otimes \mathbf{b}(\theta_0) \otimes \mathbf{a}(\theta_0)\big), \tag{5}$$

where

$$\overline{\mathbf{X}} \triangleq \text{blkdiag}\big\{\mathbf{I}_{N_\text{r}} \otimes \mathbf{X}_1^T, \ldots, \mathbf{I}_{N_\text{r}} \otimes \mathbf{X}_M^T\big\}, \tag{6}$$

and $\mathbf{d}(f_\text{d}) \triangleq [1, \ldots, e^{j2\pi(M-1)f_\text{d}T_\text{r}}]^T$ denotes the Doppler response vector. For simplicity, we define the spatial-temporal steering vector as

$$\mathbf{u}(f_\text{d}, \theta) \triangleq \mathbf{d}(f_\text{d}) \otimes \mathbf{b}(\theta) \otimes \mathbf{a}(\theta). \tag{7}$$

The spatial-temporal steering vector of the target of interest is denoted as $\mathbf{u}_0 = \mathbf{u}(f_\text{d}, \theta_0)$. Thus, the received signal vector $\mathbf{y}_0$ can be re-written in a concise form as

$$\mathbf{y}_0 = \alpha_0 \overline{\mathbf{X}} \mathbf{u}_0. \tag{8}$$

In addition to the signal reflected from the target, the radar receiver simultaneously receives unwanted clutter reflected by trees, tall buildings, cars, etc., which are generally spread in both the spatial (e.g., azimuth and range) and Doppler dimensions. Since the signal-dependent clutter is possibly stronger than the target return and deteriorates the target detection performance, it should be carefully taken into consideration in waveform designs. We assume that the clutter is generated from the CUT and $2L$ other adjacent range cells, each of which is approximated by N_c clutter patches randomly distributed in azimuth. The origin of the range coordinates is set at the target range bin.

Similar to (4), for the m-th pulse, the baseband digital samples of the return from the k-th clutter patch in the l-th range cell can be written as

$$\mathbf{Y}_{\text{c},m,l,k} = \alpha_{\text{c},l,k} e^{j2\pi(m-1)f_{\text{c},l,k}T_\text{r}} \mathbf{b}(\theta_{\text{c},l,k}) \mathbf{a}^H(\theta_{\text{c},l,k}) \mathbf{X}_m \mathbf{J}_l, \tag{9}$$

where $\alpha_{\text{c},l,k}$, $f_{\text{c},l,k}$, and $\theta_{\text{c},l,k}$ respectively denote the amplitude, Doppler frequency, and DoA of the k-th clutter patch in the l-th range cell, $k = 1, \ldots, N_\text{c}$, $l = -L, \ldots, L$, and $\mathbb{E}\big\{|\alpha_{\text{c},l,k}|^2\big\} = \sigma_\text{c}^2$. The shift matrix $\mathbf{J}_l \in \mathbb{R}^{N \times N}$ is defined by

$$\mathbf{J}_l(i,j) = \begin{cases} 1, & i - j + l = 0, \\ 0, & \text{otherwise}, \end{cases} \tag{10}$$

and $\mathbf{J}_{-l} = \mathbf{J}_l^T$. The received signal vector from the k-th clutter patch in the l-th range cell $\mathbf{y}_{\text{c},l,k} = [\text{vec}\{\mathbf{Y}_{\text{c},1,l,k}^T\}^T, \ldots, \text{vec}\{\mathbf{Y}_{\text{c},M,l,k}^T\}^T]^T$ can be expressed as

$$\mathbf{y}_{\text{c},l,k} = \alpha_{\text{c},l,k} \big(\mathbf{I}_{N_\text{r}} \otimes \mathbf{I}_M \otimes \mathbf{J}_l^T\big) \overline{\mathbf{X}} \mathbf{u}(f_{\text{c},l,k}, \theta_{\text{c},l,k}). \tag{11}$$

Defining $\overline{\mathbf{J}}_l \triangleq \mathbf{I}_{N_\text{r}} \otimes \mathbf{I}_M \otimes \mathbf{J}_l^T$ and the spatial-temporal steering vector $\mathbf{u}_{\text{c},l,k} \triangleq \mathbf{u}(f_{\text{c},l,k}, \theta_{\text{c},l,k})$ as given in (7), the clutter returns from all the clutter patches can be expressed as

$$\mathbf{y}_\text{c} = \sum_{l=-L}^{L} \sum_{k=1}^{N_\text{c}} \mathbf{y}_{\text{c},l,k} = \sum_{l=-L}^{L} \sum_{k=1}^{N_\text{c}} \alpha_{\text{c},l,k} \overline{\mathbf{J}}_l \overline{\mathbf{X}} \mathbf{u}_{\text{c},l,k}. \tag{12}$$

The clutter covariance matrix (CCM) is thus given by

$$\mathbf{R}_\text{c} = \mathbb{E}\{\mathbf{y}_\text{c} \mathbf{y}_\text{c}^H\} = \sum_{l=-L}^{L} \overline{\mathbf{J}}_l \overline{\mathbf{X}} \mathbf{M}_l \overline{\mathbf{X}}^H \overline{\mathbf{J}}_l^H, \tag{13}$$

where the inner CCM for the l-th range cell is defined by [30]

$$\mathbf{M}_l = \mathbb{E}\Big\{ \sum_{k=1}^{N_\text{c}} |\alpha_{\text{c},l,k}|^2 \mathbf{u}_{\text{c},l,k} \mathbf{u}_{\text{c},l,k}^H \Big\}. \tag{14}$$

We note that some prior work such as [25]–[27], [31] is developed based on the assumption that the spatial-temporal steering vectors $\mathbf{u}_{\text{c},l,k}$ of the clutter are known a priori, or in other words that the azimuths, ranges, and Doppler frequencies of the clutter patches are exactly known. In practice, however, it is difficult to obtain parameters such as these for the signal-dependent clutter. Thus, in this paper, we assume that only the inner CCMs $\mathbf{M}_l$ must be known (or estimated from the data), which is a more realistic assumption [32]–[34].

Denote $\mathbf{w} \in \mathbb{C}^{MNN_\text{r}}$ as the associated linear spatial-temporal receive filter whose output can be expressed as

$$r = \mathbf{w}^H \mathbf{y} = \mathbf{w}^H (\mathbf{y}_0 + \mathbf{y}_c + \mathbf{z}) \tag{15a}$$

$$= \alpha_0 \mathbf{w}^H \overline{\mathbf{X}} \mathbf{u}_0 + \mathbf{w}^H \sum_{l=-L}^{L} \sum_{k=1}^{N_\text{c}} \alpha_{\text{c},l,k} \overline{\mathbf{J}}_l \overline{\mathbf{X}} \mathbf{u}_{\text{c},l,k} + \mathbf{w}^H \mathbf{z}. \tag{15b}$$

Thus, the radar output SINR is given by

$$\text{SINR} = \frac{\sigma_0^2 |\mathbf{w}^H \overline{\mathbf{X}} \mathbf{u}_0|^2}{\mathbf{w}^H \big[\sum_{l=-L}^{L} \overline{\mathbf{J}}_l \overline{\mathbf{X}} \mathbf{M}_l \overline{\mathbf{X}}^H \overline{\mathbf{J}}_l^H + \sigma_\text{r}^2 \mathbf{I} \big] \mathbf{w}}. \tag{16}$$

In order to facilitate the discrimination between the two hypotheses in (1) for better target detection performance, the joint transmit waveform and receive filter design problem from the radar perspective aims to maximize the radar output SINR (16).

In maximizing the SINR (16), the transmit radar waveforms are subject to certain constraints due to hardware limitations and other radar sensing requirements. For notational simplicity, we define the waveform matrix in a CPI as $\mathbf{X} \triangleq [\mathbf{X}_1, \ldots, \mathbf{X}_M]$, and the waveform vector $\mathbf{x} \triangleq \text{vec}\{\mathbf{X}\}$, $\mathbf{x} = [x_1, \ldots, x_{MNN_\text{t}}]^T$. To achieve the best possible performance, we assume the total power constraint is satisfied with equality:

$$\|\mathbf{x}\|^2 = P, \tag{17}$$

where P is the total available transmit power for a CPI. Considering the hardware requirements, constant-modulus waveforms are more preferred in practical radar systems to avoid nonlinear distortion:

$$|x_i| = \sqrt{P/(MNN_\text{t})}, \quad \forall i = 1, \ldots, MNN_\text{t}. \tag{18}$$

The PAPR constraint compromises the strict constant-modulus constraint (18) by allowing power variation within a certain level and can provide a higher radar output SINR. The PAPR and its constraint are usually defined by

$$\text{PAPR} = \frac{\max\limits_{1 \le i \le MNN_\text{t}} \{|x_i|^2\}}{\|\mathbf{x}\|^2/(MNN_\text{t})} \le 1 + \varepsilon, \tag{19}$$

where $\varepsilon > 0$ is a predefined parameter to control the PAPR level. Substituting the total power constraint (17) into (19), the PAPR constraint can be re-written as

$$|x_i| \le \sqrt{(1+\varepsilon)P/(MNN_\text{t})}, \quad \forall i = 1, \ldots, MNN_\text{t}. \tag{20}$$

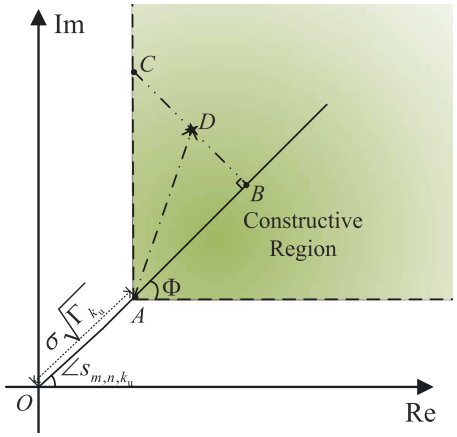

Fig. 2. CI-based SLP for QPSK constellation.

Moreover, similarity between the designed waveform and a reference waveform may also be necessary to achieve some desired ambiguity function or pulse compression properties. If we denote the reference waveform as $\mathbf{x}_0 \triangleq [x_{0,1}, \ldots, x_{0,MNN_\mathrm{t}}]^T$, the similarity constraint is formulated as

$$\|\mathbf{x}_0 - \mathbf{x}\|_\infty \leq \xi, \tag{21}$$

where ξ determines the level of allowable similarity deviation. Alternatively, the similarity constraint can be re-written as

$$|x_{0,i} - x_i| \leq \xi, \quad \forall i = 1, \ldots, MNN_\mathrm{t}. \tag{22}$$

B. User Received Signal and Communication Performance Metric

In addition to its radar sensing function, the BS also attempts to simultaneously deliver information symbols to K_u single-antenna users using the same transmit waveform. In particular, we denote the symbol vector to be transmitted by the n-th sample of the m-th pulse as $\mathbf{s}_{m,n} \triangleq [s_{m,n,1}, \ldots, s_{m,n,K_\mathrm{u}}]^T$, where each symbol is assumed to be independently selected from an Ω-phase shift keying (PSK) constellation. The waveform sample $\mathbf{x}_{m,n}$, which is the n-th column of $\mathbf{X}_m$, must be designed to carry the K_u different information symbols in $\mathbf{s}_{m,n}$. The corresponding received signal at the k_u-th user can be expressed as

$$r_{m,n,k_\mathrm{u}} = \mathbf{h}_{k_\mathrm{u}}^H \mathbf{x}_{m,n} + z_{m,n,k_\mathrm{u}}, \tag{23}$$

where $\mathbf{h}_{k_\mathrm{u}} \in \mathbb{C}^{N_\mathrm{t}}$ represents the Rayleigh fading channel between the BS and the k_u-th user, and $z_{m,n,k_\mathrm{u}} \sim \mathcal{CN}(0, \sigma^2)$ is AWGN at the k_u-th user. The nonlinear mapping from $\mathbf{s}_{m,n}$ to $\mathbf{x}_{m,n}$ is achieved by the CI-based SLP design as briefly presented below.

We use the quadrature-PSK (QPSK) constellation (i.e., $\Omega = 4$) as an example to illustrate the CI-based SLP approach as shown in Fig. 2, where $\Phi = \pi/\Omega$ is half of the angular range of the decision regions. Fig. 2 shows the case where the desired symbol of the k_u-th user is $(1/\sqrt{2}, \jmath/\sqrt{2})$, whose decision boundaries are the positive halves of x and y axes. Assume point D denotes the received noise-free signal $\widetilde{r}_{m,n,k_\mathrm{u}} = \mathbf{h}_{k_\mathrm{u}}^H \mathbf{x}_{m,n}$. Unlike conventional block-level precoding approaches aiming to eliminate the interference, the CI-based SLP approach attempts to exploit known symbol information to convert the multi-user interference into constructive components, which can enhance the communication QoS. In particular, let Γ_{k_u} be the QoS requirement of the k_u-th user. If the interference is entirely eliminated, the received noise-free signal should be at point A to satisfy $\widetilde{r}_{m,n,k_\mathrm{u}} = \sigma\sqrt{\Gamma_{k_\mathrm{u}}} s_{m,n,k_\mathrm{u}}$, i.e., $\left|\widetilde{r}_{m,n,k_\mathrm{u}}\right|^2/\sigma^2 = \Gamma_{k_\mathrm{u}}$. Instead of interference elimination/suppression, the CI-based SLP approach can utilize the interference to push the received noise-free signal deeper into the corresponding constructive (green) region, where the QoS requirement Γ_{k_u} is guaranteed and the distance between the received noise-free signal and its decision boundaries is further enlarged. Thus, lower SER and better QoS can be achieved using this CI-based SLP approach.

The relationship governing the definition of the constructive region can be geometrically expressed as $|\overrightarrow{BC}| - |\overrightarrow{BD}| \geq 0$. Due to space limitations, we omit the derivations and recommend the readers to [37]–[40] for details. The QoS constraints that guarantee that the noise-free received signal $\widetilde{r}_{m,n,k_\mathrm{u}}$ lies in the constructive region can be expressed as

$$\begin{aligned}&\Re\left\{\mathbf{h}_{k_\mathrm{u}}^H \mathbf{x}_{m,n} e^{-\jmath \angle s_{m,n,k_\mathrm{u}}} - \sigma\sqrt{\Gamma_{k_\mathrm{u}}}\right\} \sin\Phi \\ &\quad - \left|\Im\left\{\mathbf{h}_{k_\mathrm{u}}^H \mathbf{x}_{m,n} e^{-\jmath \angle s_{m,n,k_\mathrm{u}}}\right\}\right| \cos\Phi \geq 0, \quad \forall k_\mathrm{u}, m, n. \end{aligned} \tag{24}$$

In order to represent (24) in a compact form, we define

$$\begin{aligned}
\widetilde{\mathbf{h}}_{(2k_\mathrm{u}-2)MN+j}^H &\triangleq \mathbf{e}_{j,MN}^T \\
&\quad \otimes \mathbf{h}_{k_\mathrm{u}}^H e^{-\jmath \angle s_{m,n,k_\mathrm{u}}} (\sin\Phi + e^{-\jmath\frac{\pi}{2}} \cos\Phi), \\
\widetilde{\mathbf{h}}_{(2k_\mathrm{u}-1)MN+j}^H &\triangleq \mathbf{e}_{j,MN}^T \\
&\quad \otimes \mathbf{h}_{k_\mathrm{u}}^H e^{-\jmath \angle s_{m,n,k_\mathrm{u}}} (\sin\Phi - e^{-\jmath\frac{\pi}{2}} \cos\Phi), \\
\gamma_{(2k_\mathrm{u}-2)MN+j} &\triangleq \sigma\sqrt{\Gamma_{k_\mathrm{u}}} \sin\Phi, \\
\gamma_{(2k_\mathrm{u}-1)MN+j} &\triangleq \sigma\sqrt{\Gamma_{k_\mathrm{u}}} \sin\Phi,
\end{aligned}$$

where the vector $\mathbf{e}_{j,MN} \in \mathbb{R}^{MN}$ indicates the j-th column of an $MN \times MN$ identity matrix. Then, the communication QoS constraints are equivalently re-written as

$$\Re\left\{\widetilde{\mathbf{h}}_i^H \mathbf{x}\right\} \geq \gamma_i, \quad \forall i = 1, \ldots, 2K_\mathrm{u}MN. \tag{25}$$

C. Problem Formulation

In this paper, we aim to jointly design the transmit waveform $\mathbf{x}$ and the receive filter $\mathbf{w}$ to maximize the radar output SINR (16), while satisfying the communication QoS requirements (25), the total power constraint (17), and one of the waveform constraints (18), (20), or (22). Therefore, the optimization problem is formulated as

$$\max_{\mathbf{x},\mathbf{w}} \frac{\sigma_0^2 |\mathbf{w}^H \overline{\mathbf{X}} \mathbf{u}_0|^2}{\mathbf{w}^H \left[\sum_{l=-L}^{L} \overline{\mathbf{J}}_l \overline{\mathbf{X}} \mathbf{M}_l \overline{\mathbf{X}}^H \overline{\mathbf{J}}_l^H + \sigma_\mathrm{r}^2 \mathbf{I}\right] \mathbf{w}} \tag{26a}$$

$$\text{s.t. } \Re\left\{\widetilde{\mathbf{h}}_i^H \mathbf{x}\right\} \geq \gamma_i, \quad \forall i = 1, \ldots, 2K_\mathrm{u}MN, \tag{26b}$$

$$\|\mathbf{x}\|^2 = P, \tag{26c}$$

$$\mathbf{x} \in \mathcal{X}, \tag{26d}$$

where set $\mathcal{X}$ contains the feasible solutions under certain waveform constraints (18), (20), or (22), not all of which

are convex. We should emphasize that since the radar system usually requires relatively high transmit power, the communication QoS requirements (26b) are usually satisfied and thus problem (26) has a feasible solution.

It can be observed that with a fixed transmit waveform $\mathbf{x}$, the original problem (26) becomes a well-known minimum variance distortionless response (MVDR) problem [27], [31]:

$$\min_{\mathbf{w}} \ \mathbf{w}^H \Big[\sum_{l=-L}^{L} \overline{\mathbf{J}}_l \overline{\mathbf{X}} \mathbf{M}_l \overline{\mathbf{X}}^H \overline{\mathbf{J}}_l^H + \sigma_{\mathrm{r}}^2 \mathbf{I} \Big] \mathbf{w} \tag{27a}$$

$$\text{s.t. } \mathbf{w}^H \overline{\mathbf{X}} \mathbf{u}_0 = 1. \tag{27b}$$

The closed-form optimal solution $\mathbf{w}^\star$ in this case can be easily obtained as

$$\mathbf{w}^\star = \frac{\big[\sum_{l=-L}^{L} \overline{\mathbf{J}}_l \overline{\mathbf{X}} \mathbf{M}_l \overline{\mathbf{X}}^H \overline{\mathbf{J}}_l^H + \sigma_{\mathrm{r}}^2 \mathbf{I} \big]^{-1} \overline{\mathbf{X}} \mathbf{u}_0}{\mathbf{u}_0^H \overline{\mathbf{X}}^H \big[\sum_{l=-L}^{L} \overline{\mathbf{J}}_l \overline{\mathbf{X}} \mathbf{M}_l \overline{\mathbf{X}}^H \overline{\mathbf{J}}_l^H + \sigma_{\mathrm{r}}^2 \mathbf{I} \big]^{-1} \overline{\mathbf{X}} \mathbf{u}_0}. \tag{28}$$

Unlike the cyclic optimization algorithms of [25]- [27], we propose to directly optimize the joint transmit waveform and receive filter by substituting $\mathbf{w}^\star$ into the original optimization problem (26), which leads to the concentrated transmit waveform design problem:

$$\min_{\mathbf{x}} - \mathbf{u}_0^H \overline{\mathbf{X}}^H \Big[\sum_{l=-L}^{L} \overline{\mathbf{J}}_l \overline{\mathbf{X}} \mathbf{M}_l \overline{\mathbf{X}}^H \overline{\mathbf{J}}_l^H + \sigma_{\mathrm{r}}^2 \mathbf{I} \Big]^{-1} \overline{\mathbf{X}} \mathbf{u}_0 \tag{29a}$$

$$\text{s.t. } \Re\big\{ \widetilde{\mathbf{h}}_i^H \mathbf{x} \big\} \geq \gamma_i, \quad \forall i, \tag{29b}$$

$$\|\mathbf{x}\|^2 = P, \tag{29c}$$

$$\mathbf{x} \in \mathcal{X}. \tag{29d}$$

We observe that (29) is a complicated non-convex optimization problem due to the non-convex objective function (29a) and the non-convex waveform constraints (29c), (29d), which prevent a direct closed-form solution. In order to tackle these difficulties, in the following sections we employ the MM and neADMM methods to covert the waveform design problems under different constraints into tractable sub-problems, and then develop efficient algorithms to iteratively solve them.

III. Constant-Modulus Waveform Design

In this section, we focus on constant-modulus waveform design for the considered STAP-SLP-based MIMO-DFRC system by developing an MM-neADMM based algorithm. As shown in the next section, this approach can be generalized to handle the other waveform constraints discussed earlier. Substituting the constant-modulus waveform constraint (18) into (29d), the constant-modulus waveform design problem can be formulated as

$$\min_{\mathbf{x}} - \mathbf{u}_0^H \overline{\mathbf{X}}^H \Big[\sum_{l=-L}^{L} \overline{\mathbf{J}}_l \overline{\mathbf{X}} \mathbf{M}_l \overline{\mathbf{X}}^H \overline{\mathbf{J}}_l^H + \sigma_{\mathrm{r}}^2 \mathbf{I} \Big]^{-1} \overline{\mathbf{X}} \mathbf{u}_0 \tag{30a}$$

$$\text{s.t. } \Re\big\{ \widetilde{\mathbf{h}}_i^H \mathbf{x} \big\} \geq \gamma_i, \quad \forall i, \tag{30b}$$

$$|x_j| = \sqrt{P/(MNN_{\mathrm{t}})}, \quad \forall j, \tag{30c}$$

where we drop the total power constraint (29c) since the constant-modulus constraints in (30c) naturally satisfy it.

A. Reformulation

In the objective function (30a), the matrix $\overline{\mathbf{X}}$ contains the variable $\mathbf{x}$ to be optimized, but the relationship between them is not explicit. Moreover, the matrix form of $\overline{\mathbf{X}}$ is not amenable for optimization. Therefore, in order to facilitate the algorithm development, we reformulate the objective function (30a) into a more favorable expression with respect to the waveform vector $\mathbf{x}$.

Recalling the expression for $\overline{\mathbf{X}}$ in (6), we can re-write the term $\overline{\mathbf{X}}\mathbf{u}_0$ as

$$\overline{\mathbf{X}}\mathbf{u}_0 = \begin{bmatrix} \mathbf{I}_{N_{\mathrm{r}}} \otimes \mathbf{X}_1^T & & \\ & \ddots & \\ & & \mathbf{I}_{N_{\mathrm{r}}} \otimes \mathbf{X}_M^T \end{bmatrix} \begin{bmatrix} \mathbf{u}_{0,1} \\ \vdots \\ \mathbf{u}_{0,M} \end{bmatrix} \tag{31a}$$

$$= \begin{bmatrix} (\mathbf{I}_{N_{\mathrm{r}}} \otimes \mathbf{X}_1^T)\mathbf{u}_{0,1} \\ \vdots \\ (\mathbf{I}_{N_{\mathrm{r}}} \otimes \mathbf{X}_M^T)\mathbf{u}_{0,M} \end{bmatrix}, \tag{31b}$$

where $\mathbf{u}_0 = [\mathbf{u}_{0,1}^T, \ldots, \mathbf{u}_{0,M}^T]^T$ with m-th subvector $\mathbf{u}_{0,m} \in \mathbb{C}^{N_{\mathrm{t}}N_{\mathrm{r}}}$. Using the properties of the Kronecker product [42], the m-th term in (31b) can be re-arranged as

$$(\mathbf{I}_{N_{\mathrm{r}}} \otimes \mathbf{X}_m^T)\mathbf{u}_{0,m} = \mathrm{vec}\{\mathbf{X}_m^T \mathbf{U}_{0,m}\} \tag{32a}$$

$$= (\mathbf{U}_{0,m}^T \otimes \mathbf{I}_N)\mathrm{vec}\{\mathbf{X}_m^T\}, \tag{32b}$$

where the matrix $\mathbf{U}_{0,m} \in \mathbb{C}^{N_{\mathrm{t}} \times N_{\mathrm{r}}}$ is a reshaped version of $\mathbf{u}_{0,m}$ and $\mathbf{u}_{0,m} = \mathrm{vec}\{\mathbf{U}_{0,m}\}$. We can establish the following relationship between $\mathrm{vec}\{\mathbf{X}_m^T\}$ and $\mathrm{vec}\{\mathbf{X}_m\}$:

$$\mathrm{vec}\{\mathbf{X}_m^T\} = \mathbf{T}\mathrm{vec}\{\mathbf{X}_m\}, \tag{33}$$

by employing a permutation matrix $\mathbf{T} \in \mathbb{C}^{NN_{\mathrm{t}} \times NN_{\mathrm{t}}}$, which is defined by [43]

$$\mathbf{T} = \sum_{i=1}^{N_{\mathrm{t}}} \sum_{j=1}^{N} (\mathbf{e}_{j,N} \otimes \mathbf{e}_{i,N_{\mathrm{t}}})(\mathbf{e}_{i,N_{\mathrm{t}}} \otimes \mathbf{e}_{j,N})^T. \tag{34}$$

Thus, we have

$$(\mathbf{I}_{N_{\mathrm{r}}} \otimes \mathbf{X}_m^T)\mathbf{u}_{0,m} = \mathbf{A}_{0,m}\mathbf{x}_m, \tag{35}$$

where we define $\mathbf{A}_{0,m} \triangleq (\mathbf{U}_{0,m}^T \otimes \mathbf{I}_N)\mathbf{T}$ and $\mathbf{x}_m \triangleq \mathrm{vec}\{\mathbf{X}_m\}$ for brevity. Substituting (35) into (31), the term $\overline{\mathbf{X}}\mathbf{u}_0$ becomes

$$\overline{\mathbf{X}}\mathbf{u}_0 = \begin{bmatrix} \mathbf{A}_{0,1}\mathbf{x}_1 \\ \vdots \\ \mathbf{A}_{0,M}\mathbf{x}_M \end{bmatrix} = \mathbf{A}_0\mathbf{x}, \tag{36}$$

where we define $\mathbf{A}_0 \triangleq \begin{bmatrix} \mathbf{A}_{0,1} & & \\ & \ddots & \\ & & \mathbf{A}_{0,M} \end{bmatrix}$, and $\mathbf{x} \triangleq \mathrm{vec}\{\mathbf{X}\} = [\mathbf{x}_1^T, \ldots, \mathbf{x}_M^T]^T$.

Since the inner CCM $\mathbf{M}_l$ is a semi-definite matrix by its definition in (14), it can be expressed as

$$\mathbf{M}_l = \sum_{r=1}^{R_l} \lambda_{l,r} \widetilde{\mathbf{u}}_{l,r} \widetilde{\mathbf{u}}_{l,r}^H = \sum_{r=1}^{R_l} \mathbf{u}_{l,r} \mathbf{u}_{l,r}^H, \tag{37}$$

where R_l is the rank of $\mathbf{M}_l$ which generally is a small number in practice, $\lambda_{l,r}$ and $\widetilde{\mathbf{u}}_{l,r}$ are the r-th nonzero eigenvalue and its

corresponding eigenvector, respectively, and $\mathbf{u}_{l,r} \triangleq \sqrt{\lambda_{l,r}}\widetilde{\mathbf{u}}_{l,r}$. Hence, similar to the derivations in (31)-(36), we can re-write the term $\overline{\mathbf{J}}_l\overline{\mathbf{X}}\mathbf{M}_l\overline{\mathbf{X}}^H\overline{\mathbf{J}}_l^H$ as

$$\overline{\mathbf{J}}_l\overline{\mathbf{X}}\mathbf{M}_l\overline{\mathbf{X}}^H\overline{\mathbf{J}}_l^H = \sum_{r=1}^{R_l}\overline{\mathbf{J}}_l\overline{\mathbf{X}}\mathbf{u}_{l,r}\mathbf{u}_{l,r}^H\overline{\mathbf{X}}^H\overline{\mathbf{J}}_l^H \tag{38a}$$

$$= \sum_{r=1}^{R_l}\mathbf{A}_{l,r}\mathbf{x}\mathbf{x}^H\mathbf{A}_{l,r}^H \tag{38b}$$

$$\mathbf{A}_{l,r} \triangleq \overline{\mathbf{J}}_l\begin{bmatrix}\mathbf{A}_{l,r,1} & & \\ & \ddots & \\ & & \mathbf{A}_{l,r,M}\end{bmatrix}, \tag{39}$$

where $\mathbf{A}_{l,r,m} \triangleq (\mathbf{U}_{l,r,m}^T \otimes \mathbf{I}_N)\mathbf{T}$ and $\mathbf{U}_{l,r,m} \in \mathbb{C}^{N_\mathrm{t}\times N_\mathrm{r}}$ is a reshaped version of the m-th sub-vector of $\mathbf{u}_{l,r}$, namely $\mathbf{u}_{l,r,m} \in \mathbb{C}^{N_\mathrm{t}N_\mathrm{r}}$. Based on the results in (36) and (38b), the objective function (30a) can be equivalently re-formulated as

$$-\mathbf{x}^H\mathbf{A}_0^H\Big[\sum_{l=-L}^{L}\sum_{r=1}^{R_l}\mathbf{A}_{l,r}\mathbf{x}\mathbf{x}^H\mathbf{A}_{l,r}^H + \sigma_\mathrm{r}^2\mathbf{I}\Big]^{-1}\mathbf{A}_0\mathbf{x}. \tag{40}$$

B. MM Transformation

In order to efficiently solve the waveform design problem, we first utilize the MM method to convert it into a sequence of simpler problems to be solved until convergence. Specifically, given the obtained solution $\mathbf{x}_t$ in the t-th iteration, we attempt to construct a more tractable surrogate function that approximates the complicated non-convex objective function (40) at the current local point $\mathbf{x}_t$ and serves as an upper-bound to be minimized in the next iteration. The following lemma [44] is utilized to find a surrogate function for (40).

Lemma 1: For a positive-definite matrix $\mathbf{W}$*, the function* $-\mathbf{s}^H\mathbf{W}^{-1}\mathbf{s}$ *is concave in* $\mathbf{s}$ *and* $\mathbf{W}$*, and is therefore upper-bounded by its first-order linear expansion around* $(\mathbf{s}_t, \mathbf{W}_t)$ *as*

$$-\mathbf{s}^H\mathbf{W}^{-1}\mathbf{s} \le Tr\big\{\mathbf{W}_t^{-1}\mathbf{s}_t\mathbf{s}_t^H\mathbf{W}_t^{-1}\mathbf{W}\big\} - 2\Re\big\{\mathbf{s}_t^H\mathbf{W}_t^{-1}\mathbf{s}\big\} + c,$$

where c *is a constant term that is irrelevant to the variables.* ■

In order to utilize the findings in Lemma 1, we define following notation:

$$\mathbf{s} \triangleq \mathbf{A}_0\mathbf{x}, \tag{41a}$$

$$\mathbf{X} \triangleq \mathbf{x}\mathbf{x}^H, \tag{41b}$$

$$\mathbf{W} \triangleq \sum_{l=-L}^{L}\sum_{r=1}^{R_l}\mathbf{A}_{l,r}\mathbf{X}\mathbf{A}_{l,r}^H + \sigma_\mathrm{r}^2\mathbf{I}, \tag{41c}$$

and we write the objective function in (40) as $f(\mathbf{x}, \mathbf{X})$. Then, the surrogate function of $f(\mathbf{x}, \mathbf{X})$ at point $(\mathbf{x}_t, \mathbf{X}_t)$, where $\mathbf{x}_t$ is the obtained solution in the t-th iteration and $\mathbf{X}_t \triangleq \mathbf{x}_t\mathbf{x}_t^H$, can be calculated as in (42), as shown at the bottom of the page, where for brevity we define

$$\mathbf{b}_t \triangleq 2\mathbf{A}_0^H\Big[\sum_{l=-L}^{L}\sum_{r=1}^{R_l}\mathbf{A}_{l,r}\mathbf{X}_t\mathbf{A}_{l,r}^H + \sigma_\mathrm{r}^2\mathbf{I}\Big]^{-1}\mathbf{A}_0\mathbf{x}_t, \tag{43a}$$

$$\mathbf{D}_t \triangleq \sum_{l=-L}^{L}\sum_{r=1}^{R_l}\mathbf{G}_{t,l,r}^H\mathbf{X}_t\mathbf{G}_{t,l,r}, \tag{43b}$$

$$\mathbf{G}_{t,l,r} \triangleq \mathbf{A}_0^H\Big[\sum_{l=-L}^{L}\sum_{r=1}^{R_l}\mathbf{A}_{l,r}\mathbf{X}_t\mathbf{A}_{l,r}^H + \sigma_\mathrm{r}^2\mathbf{I}\Big]^{-1}\mathbf{A}_{l,r}. \tag{43c}$$

The constant terms c_1 and c_2 are irrelevant to the variables $\mathbf{x}$ and $\mathbf{X}$, and thus their detailed expressions are omitted. Equation (42c) is obtained by substituting $\mathbf{X} \triangleq \mathbf{x}\mathbf{x}^H$ back into (42b).

Based on above derivations, the transmit waveform design problem at point $\mathbf{x}_t$ can be formulated as

$$\min_{\mathbf{x}}\ \mathbf{x}^H\mathbf{D}_t\mathbf{x} - \Re\big\{\mathbf{b}_t^H\mathbf{x}\big\} \tag{44a}$$

$$\text{s.t. } \Re\big\{\widetilde{\mathbf{h}}_i^H\mathbf{x}\big\} \ge \gamma_i, \quad \forall i, \tag{44b}$$

$$|x_j| = \sqrt{P/(MNN_\mathrm{t})}, \quad \forall j. \tag{44c}$$

It can be observed that although the objective function (44a) is continuous and convex, problem (44) is still a non-convex problem due to the constant-modulus constraint (44c). While relaxing the non-convex equality constraint (44c) is an obvious approach, solving the problem with the relaxed constraint and then projecting the solution onto the constraint leads to a significant performance loss, so we propose to directly cope with the equality constraint by employing the neADMM method. While the classical ADMM method can only handle linear equality constraints, the new neADMM approach [45] can be applied to nonlinear equality constraints such as (44c). Therefore, we develop an neADMM-based method to solve this problem as follows.

C. neADMM Transformation

We first introduce an auxiliary variable $\mathbf{y} \triangleq [y_1, \ldots, y_{MNN_\mathrm{t}}]^T$ to decouple the convex constraint (44b) and the non-convex constraint (44c) with respect to $\mathbf{x}$, and

$$f(\mathbf{x}, \mathbf{X}) \le \mathrm{Tr}\Big\{\Big[\sum_{l=-L}^{L}\sum_{r=1}^{R_l}\mathbf{A}_{l,r}\mathbf{X}_t\mathbf{A}_{l,r}^H + \sigma_\mathrm{r}^2\mathbf{I}\Big]^{-1}\mathbf{A}_0\mathbf{x}_t\mathbf{x}_t^H\mathbf{A}_0^H\Big[\sum_{l=-L}^{L}\sum_{r=1}^{R_l}\mathbf{A}_{l,r}\mathbf{X}_t\mathbf{A}_{l,r}^H + \sigma_\mathrm{r}^2\mathbf{I}\Big]^{-1}\Big[\sum_{l=-L}^{L}\sum_{r=1}^{R_l}\mathbf{A}_{l,r}\mathbf{X}\mathbf{A}_{l,r}^H + \sigma_\mathrm{r}^2\mathbf{I}\Big]\Big\}$$

$$- 2\Re\Big\{\mathbf{x}_t^H\mathbf{A}_0^H\Big[\sum_{l=-L}^{L}\sum_{r=1}^{R_l}\mathbf{A}_{l,r}\mathbf{X}_t\mathbf{A}_{l,r}^H + \sigma_\mathrm{r}^2\mathbf{I}\Big]^{-1}\mathbf{A}_0\mathbf{x}\Big\} + c_1 \tag{42a}$$

$$= \mathrm{Tr}\big\{\mathbf{D}_t\mathbf{X}\big\} - \Re\big\{\mathbf{b}_t^H\mathbf{x}\big\} + c_2, \tag{42b}$$

$$= \mathbf{x}^H\mathbf{D}_t\mathbf{x} - \Re\big\{\mathbf{b}_t^H\mathbf{x}\big\} + c_2. \tag{42c}$$

convert problem (44) to

$$\min_{\mathbf{x},\mathbf{y}} \ \mathbf{x}^H\mathbf{D}_t\mathbf{x} - \Re\{\mathbf{b}_t^H\mathbf{x}\} \tag{45a}$$

$$\text{s.t. } \Re\{\widetilde{\mathbf{h}}_i^H\mathbf{x}\} \geq \gamma_i, \quad \forall i, \tag{45b}$$

$$|x_j| \leq \sqrt{P/(MNN_{\mathrm{t}})}, \quad \forall j, \tag{45c}$$

$$\mathbf{x} = \mathbf{y}, \tag{45d}$$

$$|y_j| = \sqrt{P/(MNN_{\mathrm{t}})}, \quad \forall j. \tag{45e}$$

To accommodate the neADMM framework, we define the feasible region of the inequality constraints (45b) and (45c) as set $\mathcal{C}$, and an indicator function $\mathbb{I}_{\mathcal{C}}$ associated with the set $\mathcal{C}$ as

$$\mathbb{I}_{\mathcal{C}}(\mathbf{x}) = \begin{cases} 0, & \mathbf{x} \in \mathcal{C}, \\ +\infty, & \text{otherwise.} \end{cases} \tag{46}$$

Then, by removing the constraints on $\mathbf{x}$ and adding the feasibility indicator function in the objective, problem (45) is transformed to

$$\min_{\mathbf{x},\mathbf{y}} \ \mathbf{x}^H\mathbf{D}_t\mathbf{x} - \Re\{\mathbf{b}_t^H\mathbf{x}\} + \mathbb{I}_{\mathcal{C}}(\mathbf{x}) \tag{47a}$$

$$\text{s.t. } \mathbf{x} = \mathbf{y}, \tag{47b}$$

$$|y_j| = \sqrt{P/(MNN_{\mathrm{t}})}, \quad \forall j, \tag{47c}$$

whose solution can be obtained by optimizing its augmented Lagrangian (AL) function. Specifically, the AL function of problem (47) is expressed as

$$\mathcal{L}(\mathbf{x},\mathbf{y},\boldsymbol{\lambda},\boldsymbol{\mu}) \triangleq \mathbf{x}^H\mathbf{D}_t\mathbf{x} - \Re\{\mathbf{b}_t^H\mathbf{x}\} + \mathbb{I}_{\mathcal{C}}(\mathbf{x}) + \frac{\rho}{2}\big\|\mathbf{x}-\mathbf{y}+\boldsymbol{\lambda}/\rho\big\|^2 + \frac{\rho}{2}\big\||\mathbf{y}|-\sqrt{P/(MNN_{\mathrm{t}})}+\boldsymbol{\mu}/\rho\big\|^2, \tag{48}$$

where $\rho > 0$ is a penalty parameter, $\boldsymbol{\lambda} \in \mathbb{C}^{MNN_{\mathrm{t}}}$ and $\boldsymbol{\mu} \in \mathbb{C}^{MNN_{\mathrm{t}}}$ are dual variables, and $|\cdot|$ is an element-wise absolute value operation. The AL function (48) is a more tractable function with multiple variables, which can be minimized by alternately updating $\mathbf{x}$, $\mathbf{y}$, $\boldsymbol{\lambda}$, and $\boldsymbol{\mu}$ as shown below.

D. Block Update

1) Update $\mathbf{x}$*:* With $\mathbf{y}$, $\boldsymbol{\lambda}$ and $\boldsymbol{\mu}$ given, the optimization problem for updating $\mathbf{x}$ is formulated as

$$\min_{\mathbf{x}} \ \mathbf{x}^H\mathbf{D}_t\mathbf{x} - \Re\{\mathbf{b}_t^H\mathbf{x}\} + \mathbb{I}_{\mathcal{C}}(\mathbf{x}) + \frac{\rho}{2}\big\|\mathbf{x}-\mathbf{y}+\boldsymbol{\lambda}/\rho\big\|^2. \tag{49}$$

According to the definition of $\mathbb{I}_{\mathcal{C}}(\mathbf{x})$ in (46), problem (49) can be equivalently transformed into a convex second-order cone programming (SOCP) problem:

$$\min_{\mathbf{x}} \ \mathbf{x}^H\mathbf{D}_t\mathbf{x} - \Re\{\mathbf{b}_t^H\mathbf{x}\} + \frac{\rho}{2}\big\|\mathbf{x}-\mathbf{y}+\boldsymbol{\lambda}/\rho\big\|^2 \tag{50a}$$

$$\text{s.t. } \Re\{\widetilde{\mathbf{h}}_i^H\mathbf{x}\} \geq \gamma_i, \quad \forall i, \tag{50b}$$

$$|x_j| \leq \sqrt{P/(MNN_{\mathrm{t}})}, \quad \forall j, \tag{50c}$$

whose optimal solution $\mathbf{x}^\star$ can be readily obtained by various off-the-shelf algorithms and optimization tools such as those proposed in [46], [47]. In addition, the algorithm [41] that employs the Lagrangian dual with the aid of the Hooke-Jeeves Pattern Search method can be utilized to offer an efficient solution.

2) Update $\mathbf{y}$*:* With fixed $\mathbf{x}$, $\boldsymbol{\lambda}$ and $\boldsymbol{\mu}$, the optimization problem for updating $\mathbf{y}$ is given by

$$\min_{\mathbf{y}} \ \frac{\rho}{2}\big\|\mathbf{x}-\mathbf{y}+\boldsymbol{\lambda}/\rho\big\|^2 + \frac{\rho}{2}\big\||\mathbf{y}|-\sqrt{P/(MNN_{\mathrm{t}})}+\boldsymbol{\mu}/\rho\big\|^2. \tag{51}$$

We observe that problem (51) is a non-convex problem due to the absolute value operation. Fortunately, problem (51) is separable in the elements of $\mathbf{y}$, and thus we can equivalently divide (51) into MNN_{t} sub-problems. The i-th sub-problem is expressed as

$$\min_{y_i} \ |y_i - a_i|^2 + \big||y_i| - b_i\big|^2, \tag{52}$$

where a_i and b_i are the i-th element of $\mathbf{x} + \boldsymbol{\lambda}/\rho$ and $\sqrt{P/(MNN_{\mathrm{t}})} - \boldsymbol{\mu}/\rho$, respectively. In order to handle the absolute value function, the objective of (52) is expanded as

$$|y_i - a_i|^2 + \big||y_i| - b_i\big|^2 \tag{53a}$$

$$= 2|y_i|^2 - 2\Re\big\{(a_i^* y_i + b_i^*|y_i|)\big\} + |a_i|^2 + |b_i|^2 \tag{53b}$$

$$= 2|y_i|^2 - 2|y_i|\Re\big\{(a_i^* e^{\jmath\angle y_i} + b_i^*)\big\} + |a_i|^2 + |b_i|^2. \tag{53c}$$

Since $|y_i| \geq 0$, we can easily obtain the optimal angle of y_i as $\angle y_i^\star = \angle a_i$. Substituting $\angle y_i^\star$ into (53c), the optimal amplitude of y_i can be obtained by solving

$$\min_{|y_i|} \ 2|y_i|^2 - 2|y_i|(|a_i| + \Re\{b_i\}), \tag{54}$$

whose optimal solution is given by $|y_i^\star| = 0.5(|a_i| + \Re\{b_i\})$. Therefore, the optimal solution to problem (52) is

$$y_i^\star = 0.5\big(|a_i| + \Re\{b_i\}\big)e^{\jmath\angle a_i}. \tag{55}$$

3) Update $\boldsymbol{\lambda}$ *and* $\boldsymbol{\mu}$*:* After obtaining $\mathbf{x}$ and $\mathbf{y}$, the dual variables $\boldsymbol{\lambda}$ and $\boldsymbol{\mu}$ are updated by

$$\boldsymbol{\lambda}^\star := \boldsymbol{\lambda} + \rho(\mathbf{x} - \mathbf{y}), \tag{56a}$$

$$\boldsymbol{\mu}^\star := \boldsymbol{\mu} + \rho\big[|\mathbf{y}| - \sqrt{P/(MNN_{\mathrm{t}})}\big]. \tag{56b}$$

Algorithm 1 Proposed MM-neADMM Algorithm for Constant-Modulus Waveform Design

Input: $\mathbf{A}_0$, $\mathbf{A}_{l,r}$, $\forall l$, $\forall r$, $\widetilde{\mathbf{h}}_i$, γ_i, $\forall i$, P, σ_{r}^2, ρ.
Output: $\mathbf{x}^\star$.
1: Initialize $\mathbf{x}$ by solving (57), $\mathbf{y} := \mathbf{x}$, $\boldsymbol{\lambda} := \mathbf{0}$, $\boldsymbol{\mu} := \mathbf{0}$.
2: **while** no convergence **do**
3: Update $\mathbf{x}$ by solving (50).
4: Update y_i, $\forall i$, by (55).
5: Update $\boldsymbol{\lambda}$ and $\boldsymbol{\mu}$ by (56).
6: **end while**
7: Return $\mathbf{x}^\star = \mathbf{x}$.

E. Summary, Initialization, and Complexity Analysis

With the above derivations, the proposed MM-neADMM algorithm for constant-modulus waveform design is straightforward and summarized in Algorithm 1. In summary, the transmit waveform $\mathbf{x}$ is obtained by iteratively updating $\mathbf{x}$, $\mathbf{y}$, $\boldsymbol{\lambda}$ and $\boldsymbol{\mu}$ via (50), (55), (56a) and (56b), respectively, until the relative increase of the achieved radar output SINR is less

than a given convergence threshold. Finally, with the obtained transmit waveform $\mathbf{x}^\star$, the optimal receive filter $\mathbf{w}^\star$ can be calculated by (28).

Since a good starting point is preferable for the proposed alternating optimization algorithm, we investigate how to properly initialize $\mathbf{x}$ before the iterations. In order to retain DoFs to maximize the radar output SINR under the given communication QoS constraints, we propose to use the intuitive approach of initializing $\mathbf{x}$ by maximizing the minimum QoS of the communication users using the available transmit power. Therefore, the optimization problem for initialization is formulated as

$$\max_{\mathbf{x}} \min_{i} \Re\{\widetilde{\mathbf{h}}_i^H \mathbf{x}\} \tag{57a}$$

$$\text{s.t. } |x_j| \le \sqrt{P/(MNN_{\mathrm{t}})}, \quad \forall j, \tag{57b}$$

where the power constraint (57b) is a relaxed convex version of the constant-modulus constraint (18) for the purpose of simplifying the solution. It is obvious that problem (57) is convex and can be efficiently solved by the interior point method, CVX, etc.

Next, we briefly analyze the computational complexity of the proposed waveform design algorithm. We assume that the typical interior point method is employed to solve the SOCP problem (50). Since problem (50) has an MNN_{t}-dimensional variable with $2K_{\mathrm{u}}MN$ linear matrix inequality (LMI) constraints and MNN_{t} second-order cone (SOC) constraints, the computational complexity to update $\mathbf{x}$ is of order $\mathcal{O}\{\ln(1/\varpi)\sqrt{(4K_{\mathrm{u}}+N_{\mathrm{t}})MN}M^2N^2N_{\mathrm{t}}(2K_{\mathrm{u}}+N_{\mathrm{t}}+2MNN_{\mathrm{t}}^2\}$ with ϖ representing the convergence threshold. The closed-form update for $\mathbf{y}$ in (55) or for $\boldsymbol{\lambda}$ and $\boldsymbol{\mu}$ in (56) requires the same order of computational complexity $\mathcal{O}\{MNN_{\mathrm{t}}\}$. Thus, the total computational complexity to solve for the waveform vector mainly depends on the update for $\mathbf{x}$, which emphasizes the need for low-complexity algorithms that handle large-scale SOCP problems.

Algorithm 2 Proposed MM-neADMM Algorithm for PAPR-Constrained Waveform Design

Input: $\mathbf{A}_0$, $\mathbf{A}_{l,r}$, $\forall l$, $\forall r$, $\widetilde{\mathbf{h}}_i$, γ_i, $\forall i$, P, σ_{r}^2, ρ.
Output: $\mathbf{x}^\star$.
1: Initialize $\mathbf{x}$, $\mathbf{y} := \mathbf{x}$, $\boldsymbol{\lambda} := \mathbf{0}$.
2: **while** no convergence **do**
3: Update $\mathbf{x}$ by solving (61).
4: Update $\mathbf{y}$ by (63).
5: Update $\boldsymbol{\lambda}$ by (56a).
6: **end while**
7: $\mathbf{x}^\star = \mathbf{x}$.

IV. Generalizations to Other Waveform Constraints

In this section, we generalize the proposed MM-neADMM algorithm when other waveform constraints such as the PAPR constraint (20) or the similarity constraint (22) are employed.

A. PAPR-Constrained Waveform Design

Substituting the PAPR constraint (20) into (29d), the waveform design problem (29) is re-formulated as

$$\min_{\mathbf{x}} -\mathbf{u}_0^H \overline{\mathbf{X}}^H \Big[\sum_{l=-L}^{L} \overline{\mathbf{J}}_l \overline{\mathbf{X}} \mathbf{M}_l \overline{\mathbf{X}}^H \overline{\mathbf{J}}_l^H + \sigma_{\mathrm{r}}^2 \mathbf{I}\Big]^{-1} \overline{\mathbf{X}} \mathbf{u}_0 \tag{58a}$$

$$\text{s.t. } \Re\{\widetilde{\mathbf{h}}_i^H \mathbf{x}\} \ge \gamma_i, \quad \forall i, \tag{58b}$$

$$|x_j| \le \sqrt{(1+\varepsilon)P/(MNN_{\mathrm{t}})}, \quad \forall j, \tag{58c}$$

$$\|\mathbf{x}\|^2 = P. \tag{58d}$$

We can observe that problem (58) is similar to the constant-modulus waveform design (30) except that all elements of $\mathbf{x}$ are jointly constrained in the equality constraint (58d), which requires some modifications to the proposed MM-neADMM algorithm framework as described below.

First, following the derivations in the previous section, we replace the objective (58a) with its surrogate function and introduce an auxiliary variable $\mathbf{y}$ to decouple the convex constraints (58b), (58c), and the non-convex total power constraint (58d):

$$\min_{\mathbf{x}} \mathbf{x}^H \mathbf{D}_t \mathbf{x} - \Re\{\mathbf{b}_t^H \mathbf{x}\} \tag{59a}$$

$$\text{s.t. } \Re\{\widetilde{\mathbf{h}}_i^H \mathbf{x}\} \ge \gamma_i, \quad \forall i, \tag{59b}$$

$$|x_j| \le \sqrt{(1+\varepsilon)P/(MNN_{\mathrm{t}})}, \quad \forall j, \tag{59c}$$

$$\|\mathbf{x}\|^2 \le P, \tag{59d}$$

$$\|\mathbf{y}\|^2 = P, \tag{59e}$$

$$\mathbf{x} = \mathbf{y}. \tag{59f}$$

Then, defining the feasible region of the constraints (59b)-(59e) as set $\mathcal{E}$ and the associated indicator function $\mathbb{I}_{\mathcal{E}}(\mathbf{x})$, the AL function of problem (59) can be expressed as

$$\mathcal{L}(\mathbf{x},\mathbf{y},\boldsymbol{\lambda}) \triangleq \mathbf{x}^H \mathbf{D}_t \mathbf{x} - \Re\{\mathbf{b}_t^H \mathbf{x}\} + \mathbb{I}_{\mathcal{E}}(\mathbf{x}) + \frac{\rho}{2}\|\mathbf{x}-\mathbf{y}+\boldsymbol{\lambda}/\rho\|^2. \tag{60}$$

We again propose to iteratively update each variable. Based on (60), the variable $\mathbf{x}$ is updated by optimizing

$$\min_{\mathbf{x}} \mathbf{x}^H \mathbf{D}_t \mathbf{x} - \Re\{\mathbf{b}_t^H \mathbf{x}\} + \frac{\rho}{2}\|\mathbf{x}-\mathbf{y}+\boldsymbol{\lambda}/\rho\|^2 \tag{61a}$$

$$\text{s.t. } \Re\{\widetilde{\mathbf{h}}_i^H \mathbf{x}\} \ge \gamma_i, \quad \forall i, \tag{61b}$$

$$|x_j| \le \sqrt{(1+\varepsilon)P/(MNN_{\mathrm{t}})}, \quad \forall j, \tag{61c}$$

$$\|\mathbf{x}\|^2 \le P, \tag{61d}$$

which is also a convex SOCP problem and can be easily solved using various existing algorithms. The optimization problem for updating the auxiliary variable $\mathbf{y}$ is formulated as

$$\min_{\mathbf{y}} \frac{\rho}{2}\|\mathbf{x}-\mathbf{y}+\boldsymbol{\lambda}/\rho\|^2 \tag{62a}$$

$$\text{s.t. } \|\mathbf{y}\|^2 = P, \tag{62b}$$

whose optimal solution is given by

$$\mathbf{y}^\star = \frac{\sqrt{P}(\mathbf{x}+\boldsymbol{\lambda}/\rho)}{\|\mathbf{x}+\boldsymbol{\lambda}/\rho\|}. \tag{63}$$

Finally, the dual variable $\boldsymbol{\lambda}$ is updated by (56a).

Given the above derivations, the proposed MM-neADMM algorithm for the PAPR-constrained waveform design is straightforward and summarized in Algorithm 2. The initialization is obtained by solving a convex problem that has the PAPR constraint (59c) and the total power constraint (59d) similar to (57). In each iteration, the variable $\mathbf{x}$ is updated by solving an $MNN_{\rm t}$-dimensional SOCP problem with $2K_{\rm u}MN$ LMI constraints and $(MNN_{\rm t}+1)$ SOC constraints, whose computational complexity is of order $\mathcal{O}\{\ln(1/\varpi)\sqrt{(4K_{\rm u}+N_{\rm t})MN+1}MNN_{\rm t}(2MNN_{\rm t}(MNN_{\rm t}+1)+2K_{\rm u}MN)\}$. The computational complexity of the closed-form update for $\mathbf{y}$ and $\boldsymbol{\lambda}$ are of the same order $\mathcal{O}\{MNN_{\rm t}\}$, which is much lower than that of updating $\mathbf{x}$.

B. Constant-Modulus and Similarity-Constrained Waveform Design

Here we investigate the waveform design taking into account both the constant-modulus constraint and the similarity constraint between the designed waveform and a given reference. Substituting the constant-modulus constraint (18) and similarity constraint (22) into (29d), the waveform design problem becomes

$$\min_{\mathbf{x}} -\mathbf{u}_0^H\overline{\mathbf{X}}^H\Big[\sum_{l=-L}^{L}\overline{\mathbf{J}}_l\overline{\mathbf{X}}\mathbf{M}_l\overline{\mathbf{X}}^H\overline{\mathbf{J}}_l^H+\sigma_{\rm r}^2\mathbf{I}\Big]^{-1}\overline{\mathbf{X}}\mathbf{u}_0 \quad (64a)$$

$$\text{s.t. } \Re\{\widetilde{\mathbf{h}}_i^H\mathbf{x}\}\geq\gamma_i,\quad \forall i, \quad (64b)$$

$$|x_j|=\sqrt{P/(MNN_{\rm t})},\quad \forall j, \quad (64c)$$

$$|x_j-x_{0,j}|\leq\xi,\quad \forall j. \quad (64d)$$

We observe that the optimization problem (64) is very similar to the constant-modulus waveform design problem (30), except for the additional tractable convex similarity constraints (64d). Thus, following the procedure in Sec. III, we first reformulate the objective function in a vector form and derive its convex surrogate function. Then, an auxiliary variable $\mathbf{y}$ is introduced to decouple the convex constraints (64b), (64d) and the non-convex equality constraint (64c) with respect to $\mathbf{x}$, as in (45). The neADMM algorithm is finally employed to iteratively update $\mathbf{x}$, $\mathbf{y}$, and the dual variables. Compared with (50), the solution for the update to $\mathbf{x}$ must consider the additional convex similarity constraint in (64d) on each element in $\mathbf{x}$. This results in an $MNN_{\rm t}$-dimensional SOCP problem with $2K_{\rm u}MN$ LMI constraints and $2MNN_{\rm t}$ SOC constraints, whose computational complexity is of order $\mathcal{O}\{\ln(1/\varpi)\sqrt{2MN(2K_{\rm u}+N_{\rm t})}M^2N^2N_{\rm t}(3MNN_{\rm t}^2+2N_{\rm t}+2K_{\rm u}\}$. The details are omitted here due to space limitations.

V. Simulation Results

In this section, we provide simulation results to show the effectiveness of the proposed joint transmit waveform and receive filter design algorithms. The following settings are assumed throughout our simulations. The BS is equipped with the same number of transmit and receive antennas $N_{\rm t}=N_{\rm r}=6$ with antenna spacing $d_{\rm t}=2\lambda$ and $d_{\rm r}=\lambda/2$, respectively. A CPI has $M=4$ pulses with the PRF $f_{\rm r}=1000$Hz, and each pulse is sampled $N=8$ times. The carrier frequency of the transmit waveform is $f_0=2.4$GHz and the noise power of the echoes is $\sigma_{\rm r}^2=0$dB. The target of interest is at the azimuth $\theta_0=0^\circ$ with a normalized Doppler frequency

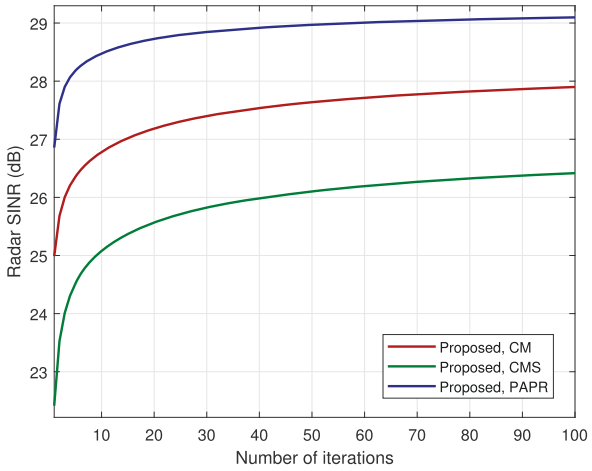

Fig. 3. Convergence illustration ($\Gamma=5$dB, $\theta_0=0$, $f_{\rm d}=0.3$, $P=30$W, $\xi=1.5\sqrt{\frac{P}{MNN_{\rm t}}}$, $\varepsilon=1$).

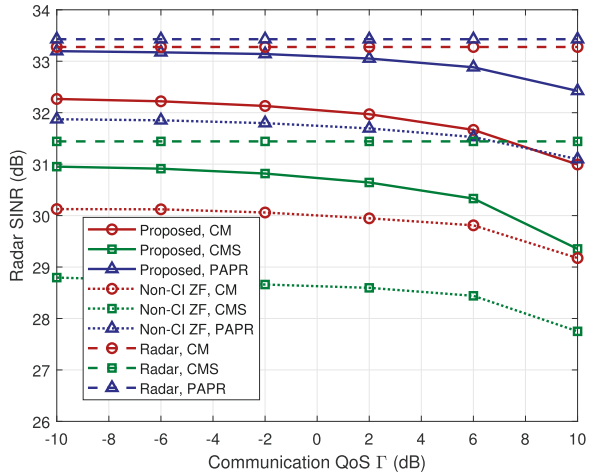

Fig. 4. Radar output SINR versus communication QoS ($\theta_0=0$, $f_{\rm d}=0.3$, $P=70$W, $\xi=1.5\sqrt{\frac{P}{MNN_{\rm t}}}$, $\varepsilon=1$).

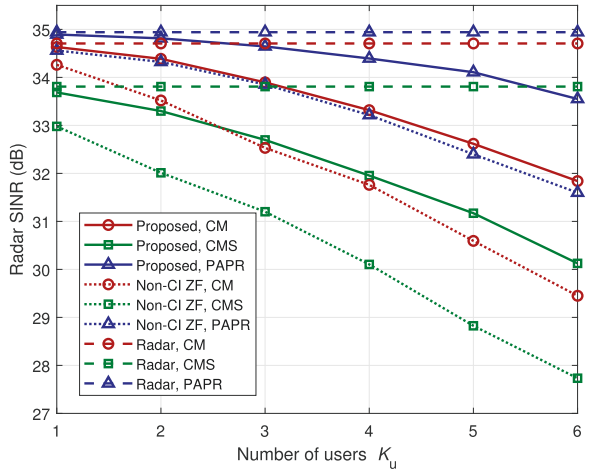

Fig. 5. Radar output SINR versus the number of users $K_{\rm u}$ ($\Gamma=5$dB, $\theta_0=0$, $f_{\rm d}=0.3$, $P=100$W, $\xi=1.5\sqrt{\frac{P}{MNN_{\rm t}}}$, $\varepsilon=1$).

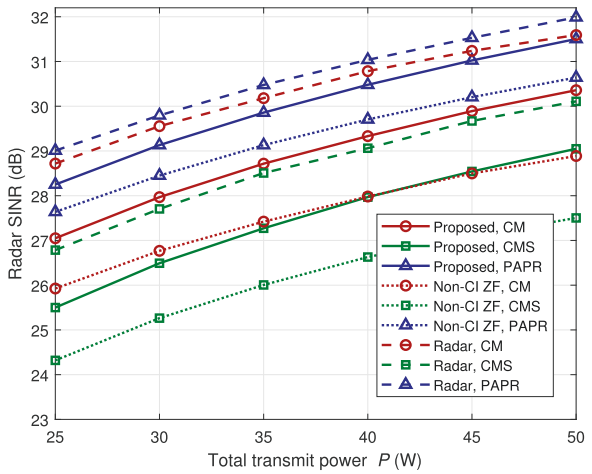

Fig. 6. Radar output SINR versus total transmit power ($\Gamma = 5$dB, $\theta_0 = 0$, $f_\mathrm{d} = 0.3$, $\xi = 1.5\sqrt{\frac{P}{MNN_\mathrm{t}}}$, $\varepsilon = 1$).

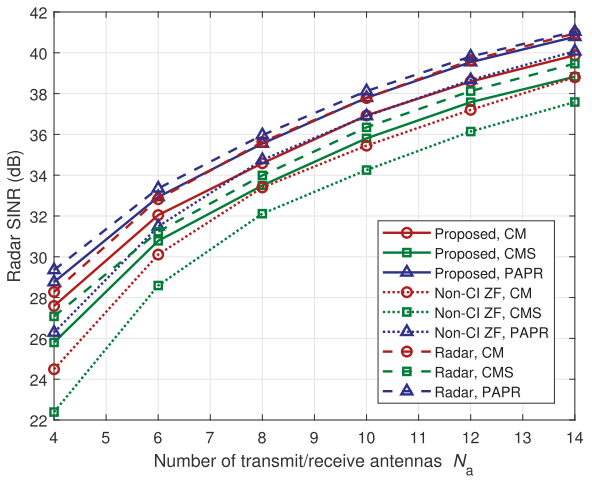

Fig. 7. Radar output SINR versus the number of antennas N_a ($\Gamma = 5$dB, $\theta_0 = 0$, $f_\mathrm{d} = 0.3$, $P = 70$W, $\xi = 1.5\sqrt{\frac{P}{MNN_\mathrm{t}}}$, $\varepsilon = 1$).

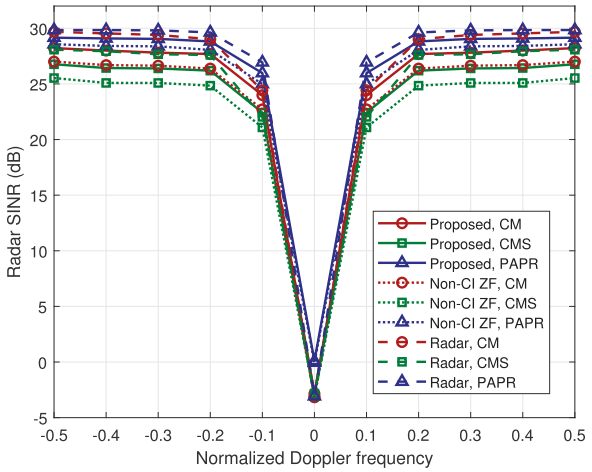

Fig. 8. Radar output SINR versus normalized Doppler frequency ($\Gamma = 5$dB, $\theta_0 = 0$, $P = 30$W, $\xi = 1.5\sqrt{\frac{P}{MNN_\mathrm{t}}}$, $\varepsilon = 1$).

$f_\mathrm{d} = 0.3$ and power $\sigma_0^2 = 0$dB unless otherwise stated. The clutter is assumed to be returned from the CUT and the nearest 4 adjacent range cells with power $\sigma_\mathrm{c}^2 = 0$dB, each of

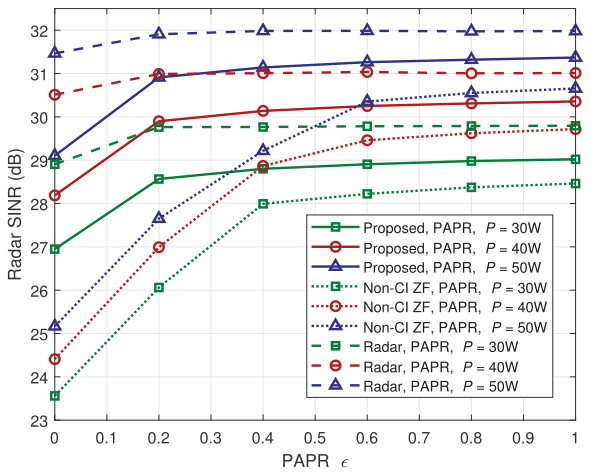

Fig. 9. Radar output SINR versus PAPR ε ($\Gamma = 5$dB, $\theta_0 = 0$, $f_\mathrm{d} = 0.3$).

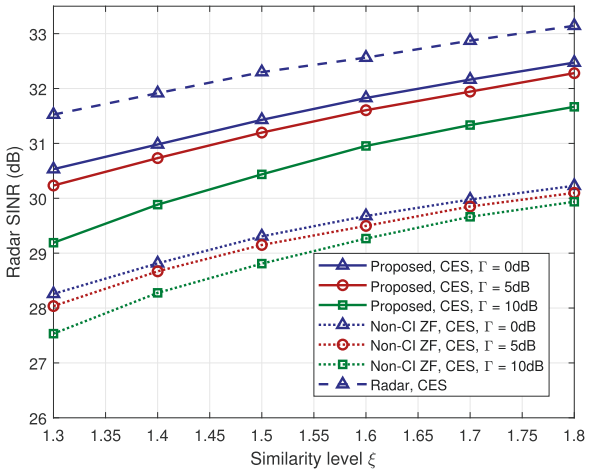

Fig. 10. Radar output SINR versus similarity level ξ ($\theta_0 = 0$, $f_\mathrm{d} = 0.3$, $P = 80$W).

which consists of $N_\mathrm{c} = 60$ clutter patches evenly distributed in azimuth. The BS also transmits information symbols to $K_\mathrm{u} = 3$ communication users, and the communication noise power is set as $\sigma^2 = -20$dB. The communication QoS for all K_u users is the same and is denoted by Γ. The penalty parameter is set as $\rho = 1$. Typical orthogonal linear frequency modulated (LFM) waveforms [20], [26], [31] are chosen as the reference waveforms since they achieve good pulse compression and ambiguity function properties. The samples of the LFM waveforms are denoted by $\mathbf{X}_0 \in \mathbb{C}^{N_\mathrm{t} \times MN}$, each element of which is given by

$$\mathbf{X}_0(i,j) = \sqrt{\frac{P}{MNN_\mathrm{t}}} \exp\{\jmath 2\pi i(j-1)/N_\mathrm{t}\} \exp\{\jmath \pi (j-1)^2/N_\mathrm{t}\},$$

and the reference waveform vector is $\mathbf{x}_0 = \mathrm{vec}\{\mathbf{X}_0\}$. In the following, the proposed DFRC waveform designs under the constant-modulus constraint, the combined constant-modulus and similarity constraints, and the PAPR constraint are referred to as "Proposed, CM", "Proposed, CMS", and "Proposed, PAPR", respectively. For comparison, the STAP-based MIMO radar-only schemes under these constraints are also included and referred to as "Radar, CM", "Radar, CMS", and "Radar,

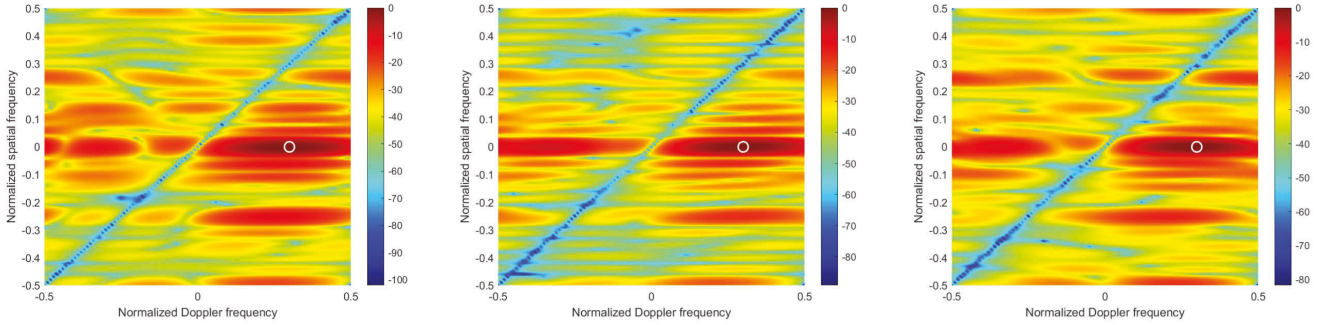

(a) Constant-modulus. (b) PAPR. (c) Constant-modulus and similarity.

Fig. 11. Space-time cross-ambiguity function under different waveform constraints ($\Gamma = 5$dB, $\theta_0 = 0$, $f_\mathrm{d} = 0.3$, $P = 30$W, $\xi = 1.5\sqrt{\frac{P}{MNN_\mathrm{t}}}$, $\varepsilon = 1$).

PAPR", respectively. In order to illustrate the advantages of the proposed CI-based SLP approach in DFRC systems, we also include the results for a zero-forcing (ZF) approach that implements the optimization of (26) with an equality constraint for the communication QoS constraint (26b). This approach, which we refer to as "Non-CI ZF", eliminates the MUI at the receivers but does not exploit it.

We first show the convergence performance of the proposed algorithms in Fig. 3, where the communication QoS is set as $\Gamma = 5$dB, the total transmit power is $P = 30$W, the similarity threshold is $\xi = 1.5\sqrt{\frac{P}{MNN_\mathrm{t}}}$, and the PAPR threshold is $\varepsilon = 1$. We see that the stricter the waveform constraint, the slower the algorithm convergence, with the PAPR constraint resulting in the fastest convergence and highest SINR, while the CMS constraint yields the slowest convergence and lowest SINR. Moreover, we see that the radar SINR monotonically increases with the iterations, which is consistent with the behavior of the MM method.

The radar output SINR versus the communication QoS requirement Γ is shown in Fig. 4. Not surprisingly, the radar output SINR achieved by the proposed MIMO-DFRC system decreases as the communication QoS requirement increases due to the trade-off between radar sensing performance and wireless communication QoS. As already noted, the PAPR-constrained waveform design achieves the highest radar SINR since it has the most relaxed waveform constraint, while the constant-modulus and similarity-constrained waveform design has the lowest radar SINR since it not only imposes the constant-modulus constraint on each transmit antenna, but also attempts to match the desired reference waveform in order to achieve other desired radar sensing properties in addition to the output SINR. The performance of the constant-modulus waveform design lies in between. In addition, we observe that the BS can provide 3 users with a communication QoS $\Gamma = 10$dB at the price of about 2dB in radar performance loss and the proposed CI-based approach has about 2dB performance improvement compared with the non-CI approach. This phenomenon confirms the advantages of utilizing STAP and CI-based SLP techniques in MIMO-DFRC systems. In Fig. 5, we present the radar output SINR versus the number of communication users. The trade-off between the radar sensing performance and the wireless communication requirement can be clearly observed. Moreover, the gap between the proposed CI-based schemes and the non-CI approaches becomes larger as K_u increases, which demonstrates the advantage of the proposed CI-based approach in exploiting MUI in dense-user cases.

Then, we illustrate the radar output SINR versus the total transmit power in Fig. 6. Clearly, a higher transmit power provides a larger radar output SINR. Moreover, the performance relationship is the same as shown in Fig. 4 and similar conclusions can be drawn. We also present the radar output SINR versus the number of antennas $N_\mathrm{a} = N_\mathrm{t} = N_\mathrm{r}$ in Fig. 7. It is clear that adding antennas achieves better performance owing to the increased waveform diversity and higher beamforming gains. Fig. 8 illustrates the radar output SINR for the proposed waveform designs under different normalized Doppler frequencies from -0.5 to 0.5. As expected, there is a significant SINR notch when the normalized Doppler frequency tends to zero, since the reflected signal from a slowly-moving target is difficult distinguish from the strong clutter returns.

In Fig. 9, we plot the radar output SINR versus the PAPR ε for different levels of total transmit power for the proposed STAP-SLP-based DFRC approach and the standard MIMO radar scheme. The radar output SINR increases with ε since the power constraint on each transmit antenna becomes less strict. Moreover, we observe that both the performance improvement and the gap between different schemes becomes smaller as ε increases. Fig. 10 illustrates the radar output SINR versus the similarity level ξ with different communication QoS constraints. The radar output SINR of all of the algorithms increases with increasing ξ considering the trade-off between the radar output SINR metric and the other radar properties endowed by the reference waveform.

Finally, in order to illustrate the capabilities of the designed DFRC waveform in target detection and clutter suppression, we plot the space-time cross-ambiguity functions of the three scenarios in Fig. 11, where the white circles denote the target location (0 normalized spatial frequency and 0.3 normalized Doppler frequency) and the number of clutter patches in each cell is set as $N_\mathrm{c} = 100$. The space-time cross-ambiguity function is defined by

$$P_{\mathbf{w},\mathbf{x}}(f_\mathrm{d},\theta) = \left|\mathbf{w}^H\overline{\mathbf{X}}\mathbf{u}(f_\mathrm{d},\theta)\right|^2. \tag{65}$$

In these colormaps, it can be seen that the mainlobes are located at the target locations while the deep nulls span the clutter ridge. This phenomenon verifies that the proposed STAP-SLP-based MIMO-DFRC system and waveform design can effectively suppress the signal-dependent clutter and achieve satisfactory target detection performance.

VI. Conclusion

In this paper, we investigated STAP and SLP-based joint transmit waveform and receive filter designs for MIMO-DFRC systems. The radar output SINR was maximized under different waveform and CI constraints that guarantee satisfactory communication QoS. Efficient algorithms exploiting MM and neADMM methods were developed to solve the resulting complicated non-convex optimization problems. Simulation examples demonstrated the advantages of utilizing STAP and CI-based SLP techniques to implement MIMO-DFRC, as well as the effectiveness of the proposed joint transmit waveform and receive filter design algorithms. Motivated by this initial work, we will further investigate other issues related to the implementation of STAP and SLP techniques in practical MIMO-DFRC systems, e.g., low-complexity algorithms, hardware imperfections, robust designs, etc.

References

[1] L. Zheng, M. Lops, Y. C. Eldar, and X. Wang, "Radar and communication co-existence: An overview," *IEEE Signal Process. Mag.*, vol. 36, no. 5, pp. 85–89, Sep. 2019.

[2] F. Liu, C. Masouros, A. P. Petropulu, H. Griffiths, and L. Hanzo, "Joint radar and communication design: Applications, state-of-the-art, and the road ahead," *IEEE Trans. Commun.*, vol. 68, no. 6, pp. 3834–3862, Jun. 2020.

[3] N. C. Luong, X. Lu, D. T. Hoang, D. Niyato, and D. I. Kim, "Radio resource management in joint radar and communication: A comprehensive survey," *IEEE Commun. Surveys Tuts.*, vol. 23, no. 2, pp. 780–814, 2nd Quart., 2021.

[4] J. A. Zhang *et al.*, "Enabling joint communication and radar sensing in mobile networks—A survey," *IEEE Commun. Surveys Tuts.*, vol. 24, no. 1, pp. 306–345, 1st Quart., 2022.

[5] F. Liu *et al.*, "Integrated sensing and communications: Towards dual-functional wireless networks for 6G and beyond," 2021, *arXiv:2108.07165*.

[6] F. Liu, C. Masouros, A. Li, T. Ratnarajah, and J. Zhou, "MIMO radar and cellular coexistence: A power-efficient approach enabled by interference exploitation," *IEEE Trans. Signal Process.*, vol. 66, no. 14, pp. 3681–3695, Jul. 2018.

[7] K. V. Mishra, M. R. B. Shankar, V. Koivunen, B. Ottersten, and S. A. Vorobyov, "Toward millimeter-wave joint radar communications: A signal processing perspective," *IEEE Signal Process. Mag.*, vol. 36, no. 5, pp. 100–114, Sep. 2019.

[8] D. Ma, N. Shlezinger, T. Huang, Y. Liu, and Y. C. Eldar, "Joint radar-communication strategies for autonomous vehicles: Combining two key automotive technologies," *IEEE Signal Process. Mag.*, vol. 37, no. 4, pp. 85–97, Jul. 2020.

[9] J. A. Zhang *et al.*, "An overview of signal processing techniques for joint communication and radar sensing," 2021, *arXiv:2102.12780*.

[10] Y. Cui, F. Liu, X. Jing, and J. Mu, "Integrating sensing and communications for ubiquitous IoT: Applications, trends, and challenges," *IEEE Netw.*, vol. 35, no. 5, pp. 158–167, Sep. 2021.

[11] H. Hua, J. Xu, and T. X. Han, "Optimal transmit beamforming for integrated sensing and communication," 2021, *arXiv:2104.11871*.

[12] A. Liu *et al.*, "A survey on fundamental limits of integrated sensing and communication," 2021, *arXiv:2104.09954*.

[13] F. Liu, C. Masouros, A. Li, H. Sun, and L. Hanzo, "MU-MIMO communications with MIMO radar: From co-existence to joint transmission," *IEEE Trans. Wireless Commun.*, vol. 17, no. 4, pp. 2755–2770, Apr. 2018.

[14] F. Liu, L. Zhou, C. Masouros, A. Li, W. Luo, and A. Petropulu, "Toward dual-functional radar-communication systems: Optimal waveform design," *IEEE Trans. Signal Process.*, vol. 66, no. 16, pp. 4264–4279, Aug. 2018.

[15] X. Liu, T. Huang, N. Shlezinger, Y. Liu, J. Zhou, and Y. C. Eldar, "Joint transmit beamforming for multiuser MIMO communications and MIMO radar," *IEEE Trans. Signal Process.*, vol. 68, pp. 3929–3944, 2020.

[16] A. Hassanien, M. G. Amin, E. Aboutanios, and B. Himed, "Dual-function radar communication systems: A solution to the spectrum congestion problem," *IEEE Signal Process. Mag.*, vol. 36, no. 5, pp. 115–126, Sep. 2019.

[17] B. Tang, H. Wang, L. Qin, and L. Li, "Waveform design for dual-function MIMO radar-communication systems," in *Proc. IEEE 11th Sensor Array Multichannel Signal Process. Workshop (SAM)*, Jun. 2020, pp. 1–5.

[18] Z. Cheng, S. Shi, Z. He, and B. Liao, "Transmit sequence design for dual-function radar-communication system with one-bit DACs," *IEEE Trans. Wireless Commun.*, vol. 20, no. 9, pp. 5846–5860, Sep. 2021.

[19] Z. Cheng, Z. He, and B. Liao, "Hybrid beamforming for multi-carrier dual-function radar-communication system," *IEEE Trans. Cognit. Commun. Netw.*, vol. 7, no. 3, pp. 1002–1015, Sep. 2021.

[20] J. Li and P. Stoica, "MIMO radar with colocated antennas," *IEEE Signal Process. Mag.*, vol. 24, no. 5, pp. 106–114, Sep. 2007.

[21] J. Qian, M. Lops, L. Zheng, X. Wang, and Z. He, "Joint system design for coexistence of MIMO radar and MIMO communication," *IEEE Trans. Signal Process.*, vol. 66, no. 13, pp. 3504–3519, Jul. 2018.

[22] P. Kumari, S. A. Vorobyov, and R. W. Heath, "Adaptive virtual waveform design for millimeter-wave joint communication—Radar," *IEEE Trans. Signal Process.*, vol. 68, pp. 715–730, 2020.

[23] W. Yuan, F. Liu, C. Masouros, J. Yuan, D. W. K. Ng, and N. Gonzalez-Prelcic, "Bayesian predictive beamforming for vehicular networks: A low-overhead joint radar-communication approach," *IEEE Trans. Wireless Commun.*, vol. 20, no. 3, pp. 1442–1456, Mar. 2021.

[24] J. R. Guerci, *Space-Time Adaptive Processing for Radar*. Norwood, MA, USA: Artech House, 2014.

[25] B. Tang and J. Tang, "Joint design of transmit waveforms and receive filters for MIMO radar space-time adaptive processing," *IEEE Trans. Signal Process.*, vol. 64, no. 18, pp. 4707–4723, Sep. 2016.

[26] G. Cui, X. Yu, V. Carotenuto, and L. Kong, "Space-time transmit code and receive filter design for colocated MIMO radar," *IEEE Trans. Signal Process.*, vol. 65, pp. 1116–1129, Mar. 2017.

[27] B. Tang, J. Tuck, and P. Stoica, "Polyphase waveform design for MIMO radar space time adaptive processing," *IEEE Trans. Signal Process.*, vol. 68, pp. 2170–2181, 2020.

[28] S. M. O'Rourke, P. Setlur, M. Rangaswamy, and A. L. Swindlehurst, "Relaxed biquadratic optimization for joint filter-signal design in signal-dependent STAP," *IEEE Trans. Signal Process.*, vol. 66, no. 5, pp. 1300–1315, Mar. 2018.

[29] S. M. O'Rourke, P. Setlur, M. Rangaswamy, and A. L. Swindlehurst, "Quadratic semidefinite programming for waveform-constrained joint filter-signal design in STAP," *IEEE Trans. Signal Process.*, vol. 68, pp. 1744–1759, 2020.

[30] G. Sun, Z. He, J. Tong, X. Yu, and S. Shi, "Mutual information-based waveform design for MIMO radar space-time adaptive processing," *IEEE Trans. Geosci. Remote Sens.*, vol. 59, no. 4, pp. 2909–2921, Apr. 2021.

[31] L. Wu, P. Babu, and D. P. Palomar, "Transmit waveform/receive filter design for MIMO radar with multiple waveform constraints," *IEEE Trans. Signal Process.*, vol. 66, no. 6, pp. 1526–1540, May 2018.

[32] G. Sun, Z. He, J. Tong, and X. Zhang, "Knowledge-aided covariance matrix estimation via Kronecker product expansions for airborne STAP," *IEEE Geosci. Remote Sens. Lett.*, vol. 15, no. 4, pp. 527–531, Apr. 2018.

[33] J. Hu, J. Li, H. Li, K. Li, and J. Liang, "A novel covariance matrix estimation via cyclic characteristic for STAP," *IEEE Geosci. Remote Sens. Lett.*, vol. 17, no. 11, pp. 1871–1875, Nov. 2020.

[34] G. Sun, M. Li, J. Tong, and Y. Ji, "Structured clutter covariance matrix estimation for airborne MIMO radar with limited training data," *IEEE Geosci. Remote Sens. Lett.*, vol. 19, pp. 1–5, 2022.

[35] C. Masouros and E. Alsusa, "Dynamic linear precoding for the exploitation of known interference in MIMO broadcast systems," *IEEE Trans. Wireless Commun.*, vol. 8, no. 3, pp. 1396–1404, Mar. 2009.

[36] C. Masouros and G. Zheng, "Exploiting known interference as green signal power for downlink beamforming optimization," *IEEE Trans. Signal Process.*, vol. 63, no. 14, pp. 3628–3640, Jul. 2015.

[37] M. Alodeh *et al.*, "Symbol-level and multicast precoding for multiuser multiantenna downlink: A state-of-the-art, classification, and challenges," *IEEE Commun. Surveys Tuts.*, vol. 20, no. 3, pp. 1733–1757, 3rd Quart., 2018.

[38] A. Li *et al.*, "A tutorial on interference exploitation via symbol-level precoding: Overview, state-of-the-art and future directions," *IEEE Commun. Surveys Tuts.*, vol. 22, no. 2, pp. 796–839, 2nd Quart., 2020.
[39] A. Li and C. Masouros, "Interference exploitation precoding made practical: Optimal closed-form solutions for PSK modulations," *IEEE Trans. Wireless Commun.*, vol. 17, no. 11, pp. 7661–7676, Sep. 2018.
[40] R. Liu, M. Li, Q. Liu, and A. L. Swindlehurst, "Joint symbol-level precoding and reflecting designs for IRS-enhanced MU-MISO systems," *IEEE Trans. Wireless Commun.*, vol. 20, no. 2, pp. 798–811, Feb. 2021.
[41] R. Liu, M. Li, Q. Liu, and A. L. Swindlehurst, "Dual-functional radar-communication waveform design: A symbol-level precoding approach," *IEEE J. Sel. Topics Signal Process.*, vol. 15, no. 6, pp. 1316–1331, Nov. 2021.
[42] R. A. Horn and C. R. Johnson, *Matrix Analysis*. Cambridge, U.K.: Cambridge Univ. Press, 1990.
[43] Y. Hardy and W.-H. Steeb, *Matrix Calculus, Kronecker Product and Tensor Product: A Practical Approach to Linear Algebra, Multilinear Algebra and Tensor Calculus With Software Implementations*, 3rd ed. Singapore: World Scientific, 2019.
[44] Y. Sun, P. Babu, and D. P. Palomar, "Majorization-minimization algorithms in signal processing, communications, and machine learning," *IEEE Trans. Signal Process.*, vol. 65, no. 3, pp. 794–816, Feb. 2017.
[45] Y. Liu, J. Zhao, M. Li, and Q. Wu, "Intelligent reflecting surface aided MISO uplink communication network: Feasibility and power minimization for perfect and imperfect CSI," *IEEE Trans. Commun.*, vol. 69, no. 3, pp. 1975–1989, Mar. 2021.
[46] F. Alizadeh and D. Goldfarb, "Second-order cone programming," *Math. Program.*, vol. 95, no. 1, pp. 3–51, 2003.
[47] S. Boyd and L. Vandenberghe, *Convex Optimization*. New York, NY, USA: Cambridge Univ. Press, 2004.

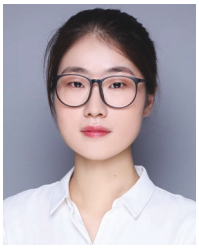

Rang Liu (Graduate Student Member, IEEE) received the B.S. degree in electronics information engineering from the Dalian University of Technology, Dalian, China, in 2018, where she is currently pursuing the Ph.D. degree with the School of Information and Communication Engineering. Her current research interests are focused on signal processing, massive MIMO systems, reconfigurable intelligent surfaces, and integrated sensing and communication. She was a recipient of the National Scholarship in 2020.

Ming Li (Senior Member, IEEE) received the M.S. and Ph.D. degrees in electrical engineering from the State University of New York at Buffalo (SUNY-Buffalo), Buffalo, in 2005 and 2010, respectively. From January 2011 to August 2013, he was a Post-Doctoral Research Associate with the Department of Electrical Engineering, SUNY-Buffalo. From August 2013 to June 2014, he joined Qualcomm Technologies Inc., as a Senior Engineer. Since June 2014, he has been with the School of Information and Communication Engineering, Dalian University of Technology, Dalian, China, where he is currently a Professor. His current research interests are in the general areas of communication theory and signal processing with applications to intelligent reflecting surface, mmWave communications, massive MIMO systems, and secure wireless communications. He is the Co-Chair of the IEEE INFOCOM 2019 Workshop on Wireless Communications and Networking in Extreme Environments.

Qian Liu (Member, IEEE) received the B.S. and M.S. degrees from the Dalian University of Technology, Dalian, China, in 2006 and 2009, respectively, and the Ph.D. degree from The State University of New York at Buffalo (SUNY-Buffalo), Buffalo, NY, USA, in 2013. She was a Post-Doctoral Fellow at the Ubiquitous Multimedia Laboratory, SUNY-Buffalo, from 2013 to 2015. She was a Post-Doctoral Fellow at the Chair of Media Technology and the Chair of Communication Networks, Technical University of Munich, from 2016 to 2017. She is currently an Associate Professor at the School of Computer Science and Technology, Dalian University of Technology. Her current research interests include multimedia transmission over MIMO systems, IEEE 802.11 wireless networks and LTE networks, device-to-device communication, energy-aware multimedia delivery, and tactile internet. She received the Best Paper Runner-up Award at the 2012 IEEE International Conference on Multimedia and Expo and was in the finalist for the Best Student Paper Award at the 2011 IEEE International Symposium on Circuits and Systems. She received the Alexander von Humboldt Fellowship in 2015.

A. Lee Swindlehurst (Fellow, IEEE) received the B.S. and M.S. degrees in electrical engineering from Brigham Young University (BYU) in 1985 and 1986, respectively, and the Ph.D. degree in electrical engineering from Stanford University in 1991. He was with the Department of Electrical and Computer Engineering, BYU, from 1990 to 2007, where he served as the Department Chair from 2003 to 2006. During 1996–1997, he held a joint appointment as a Visiting Scholar at Uppsala University and the Royal Institute of Technology, Sweden. From 2006 to 2007, he was on leave working as the Vice President of Research for ArrayComm LLC, San Jose, CA, USA. Since 2007, he has been a Professor with the Electrical Engineering and Computer Science Department, University of California at Irvine, where he worked as an Associate Dean for Research and Graduate Studies with the Samueli School of Engineering, from 2013 to 2016. During 2014–2017, he was also a Hans Fischer Senior Fellow of the Institute for Advanced Studies, Technical University of Munich. In 2016, he was elected as a Foreign Member of the Royal Swedish Academy of Engineering Sciences (IVA). His research focuses on array signal processing for radar, wireless communications, and biomedical applications, and he has over 300 publications in these areas. He received the 2000 IEEE W. R. G. Baker Prize Paper Award, the 2006 IEEE Communications Society Stephen O. Rice Prize in the Field of Communication Theory, the 2006 and 2010 IEEE Signal Processing Society's Best Paper Awards, and the 2017 IEEE Signal Processing Society Donald G. Fink Overview Paper Award. He was the Inaugural Editor-in-Chief of the IEEE JOURNAL OF SELECTED TOPICS IN SIGNAL PROCESSING.